BERGISCHE UNIVERITÄT WUPPERTAL

MASTER THESIS

Determination of the top-quark pole mass using single top-quark production cross-sections

Author:
Michael SCHUH

Supervisor:
Prof. Dr. Wolfgang WAGNER
Prof. Dr. Christian ZEITNITZ

A thesis submitted in fulfillment of the requirements for the degree of Master of Science

in the

Experimental Particle Physics
Computer Simulation in Science (CSiS)

November 7, 2016

Declaration of Authorship

I, Michael SCHUH, declare that this thesis titled, "Determination of the top-quark pole mass using single top-quark production cross-sections" and the work presented in it are my own. I confirm that:

- This work was done wholly or mainly while in candidature for a research degree at this University.
- Where any part of this thesis has previously been submitted for a degree or any other qualification at this University or any other institution, this has been clearly stated.
- Where I have consulted the published work of others, this is always clearly attributed.
- Where I have quoted from the work of others, the source is always given. With the exception of such quotations, this thesis is entirely my own work.
- I have acknowledged all main sources of help.
- Where the thesis is based on work done by myself jointly with others, I have made clear exactly what was done by others and what I have contributed myself.

Signed: _____

Date: _____

"The first principle is that you must not fool yourself — and you are the easiest person to fool. "

Richard Feynman
Surely You're Joking, Mr. Feynman!

BERGISCHE UNIVERITÄT WUPPERTAL

Abstract

Experimental Particle Physics
Computer Simulation in Science (CSiS)

Master of Science

Determination of the top-quark pole mass using single top-quark production cross-sections

by Michael SCHUH

This thesis examines the method and the applicability of an indirect top-quark mass measurement using t-channel single top-quark production cross-sections. It is argued, that the measurement strategy strongly depends on the mass dependencies of the theoretically predicted and the measured cross-sections.

Experimentally obtained results for the inclusive t-channel top-quark cross-section using the ATLAS detector are detailed and it is concluded that the mass dependence of the result lies too close to the theoretical predictions, which obstructs a sufficient top-quark mass extraction.

A research for particular sources of the mass dependence emerging from the simulation of the fiducial phase space is carried out in the second part of this work.

It is concluded that the mass dependence of the jet selection can be removed completely if the cut on the jet minimum transverse momentum in fiducial cross-section measurements can be released to a minimum of $20\,\mathrm{GeV}$.

However, this work shows that the accuracy of the indirect top-quark mass measurement from top-quark t-channel cross-sections will unlikely produce competitive results.

Acknowledgements

This work would not have been created without the great support and encouragement I received from my parents. I want to express my profound gratitude. I owe you much.

I want to thank my girlfriend for her assurance and her belief in me and for an unsurpassed time during my master studies.

I thank my friends for their support and for running all the kilometres with me.

I thankfully acknowledge that the people of the group for experimental particle physics at the University of Wuppertal where always there to help me, thank you for your time and patient advice.

In particular, I am grateful to Prof. Dr. Wagner for being the first supervisor for this thesis and for teaching me a lot and to Prof. Dr. Zeitnitz for his effort as the second supervisor.

Contents

List of Figures

List of Tables

List of Abbreviations

ATLAS	**A** **T**oroidal **L**HC **A**pparatu**S**
CKM	**C**abibbo-**K**obayashi-**M**askawa
CMS	**C**ompact **M**uon **S**olenoid
CSC	**C**athode **S**trip **C**hambers
FSR	**F**inal **S**tate **R**adiation
HATHOR	**Ha**dronic **T**op and **H**eavy quarks cross-section calculat**OR**
HLT	**H**igh **L**evel **T**rigger
ID	**I**nner **D**etector
ISR	**I**nitial **S**tate **R**adiation
LHAPDF	The **L**es **H**ouches **A**ccord **P**arton **D**ensity **F**unctions
LHC	**L**arge **H**adron **C**ollider
LHCb	**L**arge **H**adron **C**ollider **b**eauty
LO	**L**eading **O**rder
MCFM	**M**onte **C**arlo for **FeM**tobarn processes
ME	**M**atrix **E**lement
MDT	**M**onitored **D**rift **T**ubes
NLO	**N**ext-to-**L**eading **O**rder
NNLO	**N**ext-to-**N**ext-to-**L**eading **O**rder
PDF	**P**arton **D**ensity **F**unction
PS	**P**arton **S**hower
QCD	**Q**uantum **C**hromo **D**ynamic
QED	**Q**uantum **E**lectro **D**ynamic
SCT	**S**ilicon **S**trip **T**racker
TRT	**T**ransition **R**adiation **T**racker

List of Symbols

$\hbar$	Planck Constant	set to 1
c	Speed of Light	set to 1
G_F	Fermi constant	$1.663787(6) \cdot 10^{-5}\,\mathrm{GeV}^{-2}$
α_e	QED coupling constant	$1/132.2332298$
$\alpha_s(M_Z)$	QCD coupling constant	0.1183 ± 0.0016
Λ_{QCD}	QCD scale	$217^{+25}_{-23}\,\mathrm{MeV}$
$m(W)$	W-boson mass	$80.403\,\mathrm{GeV}$
$m(Z)$	Z-boson mass	$91.1876\,\mathrm{GeV}$
$m(t)$	top-quark reference mass	$172.5\,\mathrm{GeV}$
$sin^2(\theta_W)$	weak mixing angle squared	0.2228972

1. Introduction

The successful LHC runs and the increasing amount of collected data constitute a range of new possibilities for particle physics and especially for top-quark research. Higher order cross-section studies based on improved theoretical calculations allow precise tests of the underlying theory the Standard Model of Particle Physics (SM). In addition to the inclusive measurements, differential analysis of single top-quark production cross-sections as functions of transverse momentum and the absolute rapidity of the top-quark decay particles become seizable with the rising luminosity. In the case of $t\bar{t}$-pairs this even extends to first double differential analysis.

Direct reconstruction methods have delivered high precision measurements of the top-quark mass that are needed to reduce the uncertainties of many parameters of the SM. Cross-section measurements can be used to determine the top-quark mass indirectly by superimposing the experimentally obtained result onto the theoretically constructed distribution. Although this technique does not reach the accuracy of direct measurements, it provides a stringent test of the self-consistency of the theory.

In general, the experimental results depend on the top-quark mass m_t^{MC}, modelled in a running mass scheme, as an input parameter for MC event generators, whereas the theoretical calculations depend on the top-quark mass modelled in a pole mass scheme. Quantitative studies have justified the identification of m_t^{MC} with m_t^{pole} within an uncertainty of $\mathcal{O}(\Lambda_{\mathrm{QCD}})$ [1, 2]. However, the driving factor for the accuracy that can be achieved with the indirect top-quark mass extraction are neither the experimental nor the theoretical uncertainties, but the difference between the experimental and theoretical top-quark mass dependencies. An orthogonal dependence would maximise the accuracy, while a parallel dependence would obstruct the method's applicability.

For $t\bar{t}$ cross-sections in NNLO calculation the top-quark mass extraction has been performed by ATLAS [3] and CMS [4]. For an overview see [5, 6]. The lowest top-quark mass dependence of measured $t\bar{t}$ cross-sections has been achieved with the ATLAS detector at 7 and $8\,\mathrm{TeV}$ corresponding to a derivative of $^{d\sigma_{t\bar{t}}}/_{dm_t} = -0.28\,\%/\mathrm{GeV}$ at $m_t = 172.5\,\mathrm{GeV}$. D$\varnothing$ has updated results for the same analysis and has reduced the mass dependence from $-1.13\,\%/\mathrm{GeV}$ in 2011 [7] to $-0.68\,\%/\mathrm{GeV}$ in 2016 [8]. This has improved the accuracy of their indirect top-quark mass measurement using $t\bar{t}$ cross-sections from a previous precision of $3\,\%$ to $1.9\,\%$. CMS results with $1.7\,\%$ lie between D$\varnothing$ and ATLAS precision, which is $1.5\,\%$ using combined 7 and $8\,\mathrm{TeV}$ data with a final result of $172.9^{+2.5}_{-2.6}\,\mathrm{GeV}$ [3].

This work presents a feasibility study of the pole mass extraction from combined results for singly produced t-channel top-quarks and top-antiquarks in pp collisions at $\sqrt{s} = 8\,\mathrm{TeV}$ that have been shown to compare about half of that of $t\bar{t}$ production [5]. In order to implement a replicable analysis for this thesis, the C++ program xHathor based on Root6, Hathor2.1

and LHAPDF6 was written and used to perform the indirect mass extraction.

After outlining the current understanding of top-quark physics within the context of the SM in chapter 2, the xHathor program and the theoretical cross section prediction with Hathor v2.1 and LHAPDF6.1.6 is explained in chapter 3. A detailed discussion of the method of extracting the top-quark mass from the combination of theoretically and experimentally obtained cross-section measurements is given in chapter 4. In chapter 5, the method is applied to the fiducial cross-section measurement result obtained with the ATLAS detector.

This analysis shows that the current single top-quark t-channel cross-section measurement depends too strongly on the top-quark mass. Superimposed on the theoretical prediction, this yields almost parallel curves, which does not allow a precise top-quark mass measurement. A research for the mass dependence grounded on the fiducial measurement technique is presented in chapter 6. Ways to reduce this mass dependence within the process of event selection are proposed in chapter 7 and a conclusion that seeks to contribute to more accuracy in the indirect top-quark mass measurement is drawn in chapter 8.

2. Top-quark physics

2.1 The Standard Model of Particle Physics

The Standard Model of Particle Physics is a perturbatively renormalisable gauge quantum field theory that incorporates subatomic elementary particles and fundamental interactions between them in the gauge group SU$(3)\times$ SU$(2)\times$SU(1). The Lagrangian density embodies a quantum electro-dynamic sector (QED) and a quantum chromo-dynamic sector (QCD) with the respective electro-magnetic and weak hypercharge gauge field tensors and the gluon gauge field tensor. The strong or coloured interaction is represented by the colour symmetry group SU(3) that is generated by the Gell-Mann matrices. The electro-dynamic symmetry group unifies the electro magnetic and weak interaction in the Lie group SU$(1)\times$ SU(2). Gauge bosons are force carrier particles that correspond to excitations of the gauge field and that intermediate interactions of strong, weak and electro-magnetic type. The eight massless gluons are self-coupling QCD bosons that interact between the colour-charged quarks. The massless photon is the QED boson that interacts between electrically charged particles. The neutral Z and the electrically charged W^+ and W^- bosons intermediate the weak force that explains radioactive decay and interacts between all fermions including all quarks and leptons. In contrast to photons and gluons they have significant masses that are only outweighed by the Higgs boson and the top-quark. $W^\pm$ bosons only interact with left-handed particles and right-handed antiparticles, whereas the Z boson does interact without regard to the chirality. The generation of the gauge boson masses due to spontaneous breaking of the weak isospin symmetry of the electroweak interaction is explained in the SM by the Brout–Englert–Higgs mechanism. The Higgs field sector of the Lagrangian density of the SM describes a complex scalar field of the SU(2) group that is non-zero at every point in space-time. An electrically neutral component explains the fermion masses due to Yukawa coupling. The Higgs boson has integer spin 0, which makes it unique among the particles of the SM and distinguishes it from force carrier bosons that have integer spin 1 and from fermions that have non-integer spin $1/2$. It has been a central goal of the LHC agenda to prove the existence of the electrical and colour-neutral Higgs boson. It has been observed at the LHC with a mass of approximately $126\,\mathrm{GeV}$ [9].

The SM depends on 19 experimentally determined parameters, amongst them the masses of the six quarks and of the electron, muon and tau lepton, but it does not include neutrino masses. Additionally, it neither explains dark matter nor dark energy as integrated into the Standard Model of Cosmology. It also falls short to include the theory of gravitation that is described by general relativity.

The six quark flavours and six leptonic particles are arranged in the scheme in figure 2.1. The first row lists the up-type quarks u (up), c (charm) and the top-quark t. The second row shows the down-type quarks d (down),

s (strange) and the bottom-quark b. Antiquarks are denoted as $(\bar{u}, \bar{d}, \bar{s}, \bar{c}, \bar{b}, \bar{t})$; they have same masses and mean life time and the same spin but opposite sign in all charges. The electric charge is summed by the third component I_3 of the weak isospin and the weak hypercharge Y_W obeying $Q = I_3 + {}^{Y_W}/_2$. For up-type quarks it holds that $I_3 = {}^1/_2$ and for down-type quarks it holds that $I_3 = -{}^1/_2$. The weak hypercharge is given as $Y_W = {}^1/_3$ for all left-handed quarks. For particles with right-handed chirality the third component of the weak isospin is zero.

Composite particles that have a quark substructure are called hadronic. Mesons are unstable hadrons that contain one quark and their antiquark. Stable atomic matter is composed of Baryons that contain three quarks where all three colour charges red, green and blue or their respective anti-colours are present. Protons contain two up-quarks and a down-quark; neutrons contain two down-quarks and one up-quark. Aside these so-called valence quarks that enter the quantum number determination, hadrons contain gluons and sea quarks that appear as pairs of quarks of different flavour.

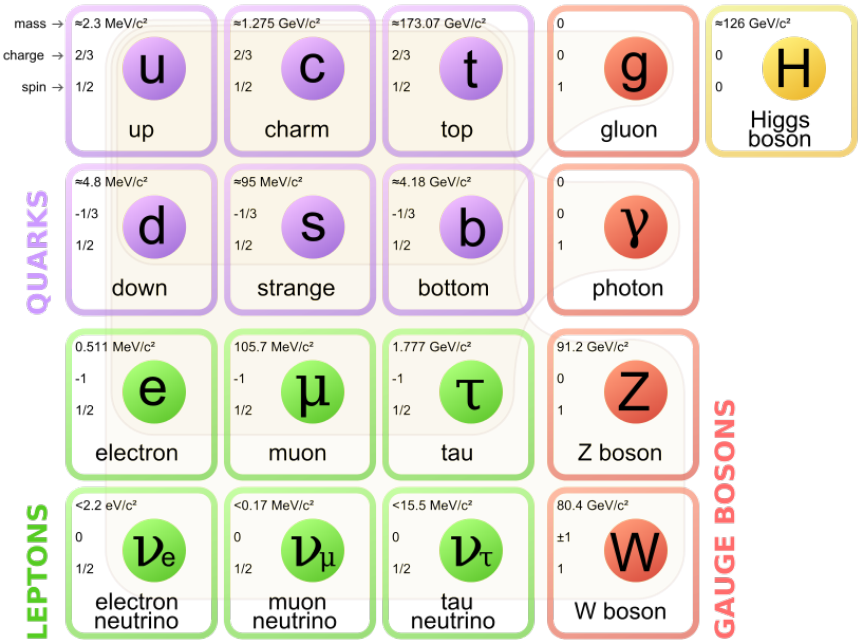

FIGURE 2.1: The elementary particles included in the Standard Model of Particle Physics. Fermions are arranged in three generations. All particles aside the massless photon and gluon are shown indicating their mass in MeV or GeV since $c^2 = 1$ is used in particle physics.
source: [10]

2.2 The top-quark mass and decay

The existence of the top-quark as a part of the weak isospin doublet together with the b-quark was predicted early 1973 by M. Kobayashi and T. Maskawa at the time of the finding of the theory of strong interaction (QCD) [11]. Like all particles of the second and third generation, which are contained in the second and third column in the scheme given in figure 2.1, it is

unstable and like all quarks except the stable up-quark it decays via flavour changing weak interaction.

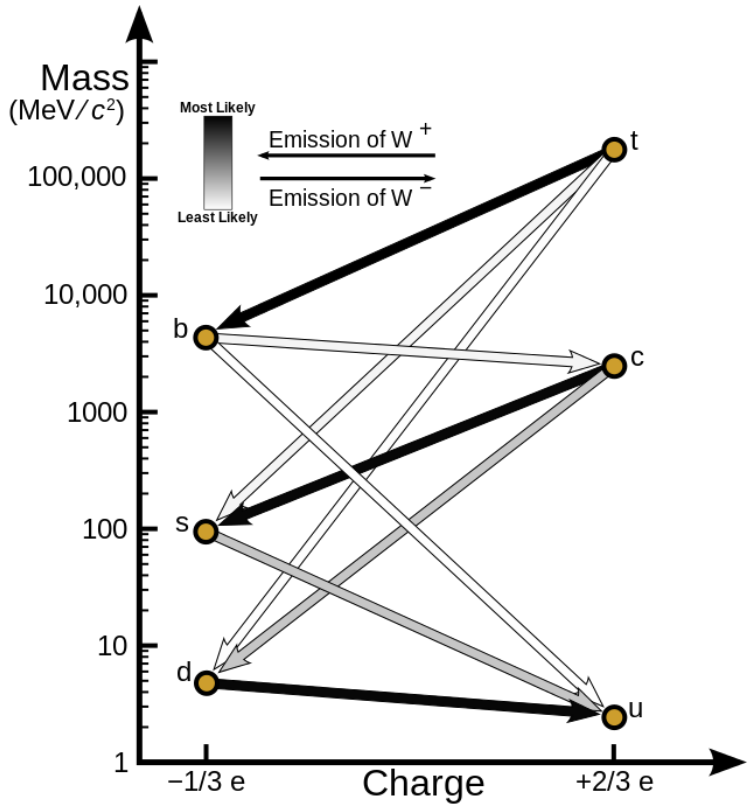

FIGURE 2.2: Flavour changing weak quark decays. The coupling probabilities are given by the CKM matrix parameters. The top-quark decays almost exclusively to a bottom-quark.
source: [12]

Figure 2.2 visualises the involved processes. The grey scales of the arrows indicate the likelihoods of the decay paths that each correspond to the absolute value of an entry in the Cabibbo-Kobayashi-Maskawa (CKM) matrix as given by equation 2.1 [13]. This observation, known as quark mixing, can be related to three mixing angles, which together with a complex CP-violating phase add four parameters to the SM.

$$\begin{bmatrix} |V_{ud}| & |V_{us}| & |V_{ub}| \\ |V_{cd}| & |V_{cs}| & |V_{cb}| \\ |V_{td}| & |V_{ts}| & |V_{tb}| \end{bmatrix} \approx \begin{bmatrix} 0.97434 \pm 0.00012 & 0.22506 \pm 0.0005 & 0.00357 \pm 0.00015 \\ 0.22492 \pm 0.0005 & 0.97343 \pm 0.00013 & 0.0411 \pm 0.0013 \\ 0.00875 \pm 0.00033 & 0.0403 \pm 0.0013 & 0.99915 \pm 0.00005 \end{bmatrix} \quad (2.1)$$

The main-diagonal of the CKM matrix reveals that quarks preferably change flavour within one generation and $|V_{tb}| \approx 1$ shows that the top-quark does almost exclusively decay to a W boson and a bottom-quark. The top-quark decay gives experimental access to the vector-axial-structure of the Wtb-vertex and constructs a way to directly measure $|V_{tb}|$, which is independent of the number of quark generations and the unitarity of the CKM matrix. Constraints on $|V_{tb}|$ support a range of tests of the Standard Model, notably the CP-violation in weak decays that is explained by the complex phase of the CKM matrix. Further constrained by the unitarity

of the CKM matrix, the result is usually quoted as a lower limit. Couplings of the top-quark to lighter quarks are strongly suppressed and are not expected to be directly accessible using tree-level processes involving top quarks. Alternatives exist with $B - \bar{B}$ oscillations, which are mediated by box diagrams involving top-quarks and with rare K and B decays, which involve top-quark loops [13].

The mass of the top-quark is a very precisely measured quantity and new methods to further decrease the uncertainty on its experimentally obtained value are currently under development. The combined result achieved by the LHC detectors ATLAS and CMS using up to $4.9\,\mathrm{fb}^{-1}$ data taken at $7\,\mathrm{TeV}$ has a precision of $0.56\,\%$ [14] and the Tevatron average contributed by the D∅ and CDF experiments at $1.96\,\mathrm{TeV}$ using up to $9.7\,\mathrm{fb}^{-1}$ data reports a precision of $0.37\,\%$ [15]. The LHC - Tevatron combination based on these results reaches $0.44\,\%$ accuracy and reads $m_t = 173.34 \pm 0.27(\mathrm{stat}) \pm 0.71(\mathrm{syst})\,\mathrm{GeV}$ with a total uncertainty of $0.76\,\mathrm{GeV}$ [16].

This value is large enough to be indirectly accessible and expectations were expressed [17] well before the top-quark was first observed in $p\bar{p}$-collisions at the Tevatron by the CDF and D∅ collaborations in 1995 [18, 19]. One example are $B^0\bar{B}^0$ mixing experiments by ARGUS at DESY in 1986, in which a lower limit was concluded due to the dependency of observables on $m_t^2 - m_c^2$.

The top-quark has an extremely short lifetime with a decay width that is expressed in NLO at order $\mathcal{O}(\alpha_s)$ by equation 2.2 [20].

$$\Gamma = \frac{G_F}{8\pi\sqrt{2}} m_t^3 \left(1 - \frac{M_W^2}{m_t^2}\right)^2 \left(1 + 2\frac{M_W^2}{m_t^2}\right) \left[1 - \frac{2\alpha_s}{3\pi}\left(\frac{2\pi^2}{3} - \frac{5}{2}\right)\right] \tag{2.2}$$

This yields a narrow decay width below $\Gamma \approx 1.5\,\mathrm{GeV}$ and corresponds to the lifetime given in equation 2.3, which is smaller than the time span t_{had} needed for hadronisation.

$$\tau_t \approx 1.5 \cdot 10^{-25}\,\mathrm{s} < t_{\mathrm{had}} \approx \frac{1}{\Lambda_{\mathrm{QCD}}} \approx 3 \cdot 10^{-24}\,\mathrm{s} \tag{2.3}$$

In contrast to lighter quarks which all recombine to bound states, the top-quark thus decays as a free particle and its polarisation, which can be calculated in perturbation theory, is directly transferred to its decay products. The spin of the top-quark is $100\,\%$ correlated to the helicity fractions of the W boson, to the angular distribution of the leptonic decay particles of the W-boson and to other dependent observables [21, 22].

Being the heaviest known elementary particle, the top quark's Yukawa coupling to the Higgs boson is of order of unity and it is the only quark with a mass at the order of the electroweak energy scale. This is particularly considerable as it introduces large loop corrections to SM calculations and makes the top-quark mass a crucial input for Higgs boson mass expectations and other predictions of the SM. An example, studied by CMS and LHCb experiments, are very rare decays of B-mesons to two muons that can be predicted from the SM with very small branching ratios $\mathcal{B}(B_s^0 \to \mu^+\mu^-) = (3.66 \pm 0.23) \cdot 10^{-9}$ and $\mathcal{B}(B^0 \to \mu^+\mu^-) = (1.06 \pm 0.09) \cdot 10^{-10}$. Feynman graphs of these strongly loop suppressed processes involving top-quark loops are presented in [23]. This is extended to the search for

new physics beyond the Standard Model by assumption of the existence of top-quark loops together with yet unknown particles.

Another prominent example concerns studies about the stability of the electroweak vacuum that depends on the running of the parameter $\lambda(Q^2)$ of the Higgs potential. Precision measurements of the top-quark mass affect related discussions whether the metastability or stability can be shown within the SM without assuming the presence of new physics below the Plank Scale [24, 25, 26].

2.3 Single top-quark production

Due the top quark's heavy mass and the implicated production threshold, the only machines capable to produce top-quarks are the Tevatron that ceased operation in 2011 and the LHC that started operation in 2010. The highest production rates are observed in top-quark-antiquark pair-production that is mediated by strong interaction. In the most common processes, a highly energetic gluon is produced either via gluon-gluon-fusion or quark-antiquark annihilation that then decays into the top-quark-antiquark pair. Single top-quark production, in contrast, involves electro-weak charged current interaction. The production rate for single top-quarks is suppressed to less than half of the rate of pair-production because of the difference in coupling strengths of the weak and strong interaction, which is partially compensated due to the lower production threshold.

At the Tevatron the $p\bar{p}$-collisions represented an initial CP eigenstate and no significant difference between single top-quark and single top-antiquark cross-sections was observable. This is different for pp-collisions at the LHC, where a ratio of about 65% top-quarks and 35% top-antiquarks is observed at $8\,\mathrm{TeV}$. Notably, antiquarks in pp-collisions can only be sea-quarks but none of the three quantum-numbers determining valence quarks in each proton.

Single top-quark production is classified into three production channels that are discriminated by the virtuality $Q^2 = -q^2$ of the W-boson at the Wtb-vertex, which is the negative of the four-momentum q^2 of the W-boson. The processes that involve the exchange of a virtual W-boson are the t-channel with a space like W-boson ($q^2 < 0$) and s-channel with a time like W-boson ($q^2 \geq (m_t + m_b)^2$). Their Feynman graphs are shown in figure 2.3. The ratio between t and s-channel allows to probe the SM and conclusions from a variety of proposed extensions of the SM [27]. The processes that result in a real W-boson ($q^2 = m_W^2$) in addition to a top-quark in the final state are known as associated tW-production or tW-channel. The two respective Feynman graphs are drawn in figure 2.4.

The t-channel $qb \to q't$ and $\bar{q}b \to \bar{q}'t$ is the most abundant of the three production processes. The most frequent sub-processes involve a light quark q inside one proton and a b quark in the other, leading to the exchange of a space-like virtual W-boson and the emission of a light quark alongside the top-quark. The processes in which a second generation charm-quark hits the b-quark or a second generation strange-quark is produced together with the top-quark are Cabibbo suppressed. The same is valid for negligible contributions from processes in which a lighter quark replaces the b-quark.

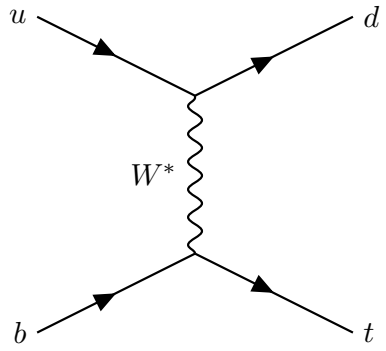

(a) Tree level process in the t-channel. Combined cross-sections are denoted as $\sigma(tq+\bar{t}q)$.

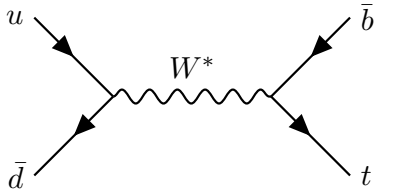

(b) Tree level process in the s-channel. Combined cross-sections are denoted as $\sigma(t\bar{b}+\bar{t}b)$.

FIGURE 2.3: Leading order Feynman Diagrams for (a) t-channel and (b) s-channel. These are the processes featuring timelike (a) and spacelike (b) virtual W-bosons and produce two quarks in the final state.

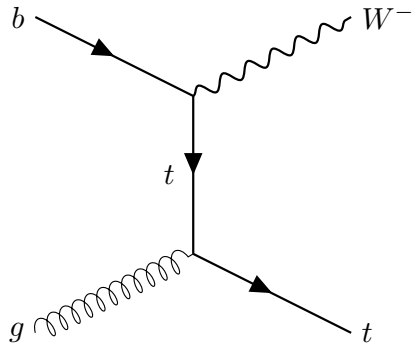

(a) Diagram for the $gb \rightarrow tW^-$ process.

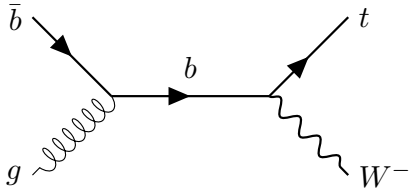

(b) Diagram for the $g\bar{b} \rightarrow tW^-$ process.

FIGURE 2.4: Leading order Feynman Diagrams for associated tW-production. Combined cross-sections are denoted as $\sigma(tW + \bar{t}W)$. These are the processes featuring a real on-shell W-boson.

The process underlying the s-channel production involves an initial quark-antiquark annihilation $q\bar{q}' \to t\bar{b}$ followed by the decay of a time-like virtual W-boson, which produces a top-quark and a bottom-antiquark. Because the initial state consists of a quark and an antiquark, this channel exhibits different production rates in proton-proton-collisions compared to proton-proton-collisions at the same centre-of-mass energy. Due to the absence of NLO contributions that are enhanced by the higher gluon luminosity at LHC energies, s-channel production increases less strongly than t-channel production.

Associated tW-production $gb \to tW$ involves a gluon even in LO diagrams and supersedes the s-channel at the LHC, while at Tevatron energy scale this cross-section was negligibly small. Contributions involving first and second generation down-type quarks instead of the b-quark are strongly Cabibbo suppressed.

For all three single top-quark production processes the cross-sections have been approximately calculated at aNNLO in perturbation theory and the NLO QCD corrections are known including also the decay of the top-quark [28, 29, 30, 31]. For t-channel production the theoretical predictions have been extended recently to NNLO results [32]. Theoretical cross-section calculation is discussed in more detail in chapter 3. Figure 2.5 shows the expectations within estimated uncertainties for pp-collisions and $p\bar{p}$-collisions for all three channels and displays experimental results at four different energies as published between 2010 and 2015. Experimental single-top-quark data-taking with the ATLAS detector is discussed in detail in chapter 5. Figure 2.6 shows the state of the art of ATLAS measurements and compares results to expectations.

The Tevatron experiments first reported evidence for t-channel collisions at a late phase of run II in 2009, 14 years after they published their results on evidence of $t\bar{t}$-pair-production in 1995 [35, 36, 37, 38]. The latest update on the combined Tevatron result for an energy of $1.96\,\mathrm{TeV}$ was published 2015 and reports a combined t-channel and s-channel cross-section of $\sigma(tq + \bar{t}q + t\bar{b} + \bar{t}b) = 3.3^{+0.52}_{-0.40}\,\mathrm{pb}$ [39]. In the LHC era single top-quark production has evolved to significantly higher rates with latest results that read $\sigma(tq) = 156 \pm 5(\text{stat.}) \pm 27(\text{syst.}) \pm 3(\text{lumi.})\text{pb}$ and $\sigma(\bar{t}q) = 91 \pm 4(\text{stat.}) \pm 18(\text{syst.}) \pm 2(\text{lumi.})\text{pb}$ for the ATLAS measurement using $3.2\,\mathrm{fb}^{-1}$ of $13\,\mathrm{TeV}$ data [40].

While early measurements had less statistics and measured only inclusive cross sections, LHC run II now produces enough luminosity to perform differential analysis of single top-quark cross-sections as functions of the transverse momentum and the absolute value of the rapidity of the top-quark. This has recently been published by the CMS collaboration using $3.2\,\mathrm{fb}^{-1}$ of $13\,\mathrm{TeV}$ data from 2015 [41].

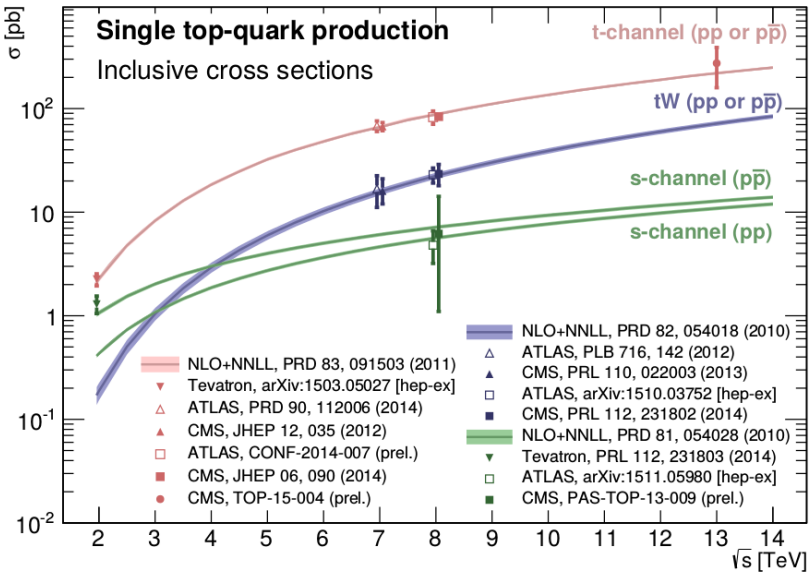

FIGURE 2.5: Single top-quark inclusive cross-section measurements of Tevatron and LHC experiments compared to theory calculations as functions of centre-of-mass energy . Predictions are based on Hathor 2.1 in NLO+NLL QCD precision.
source: [33]

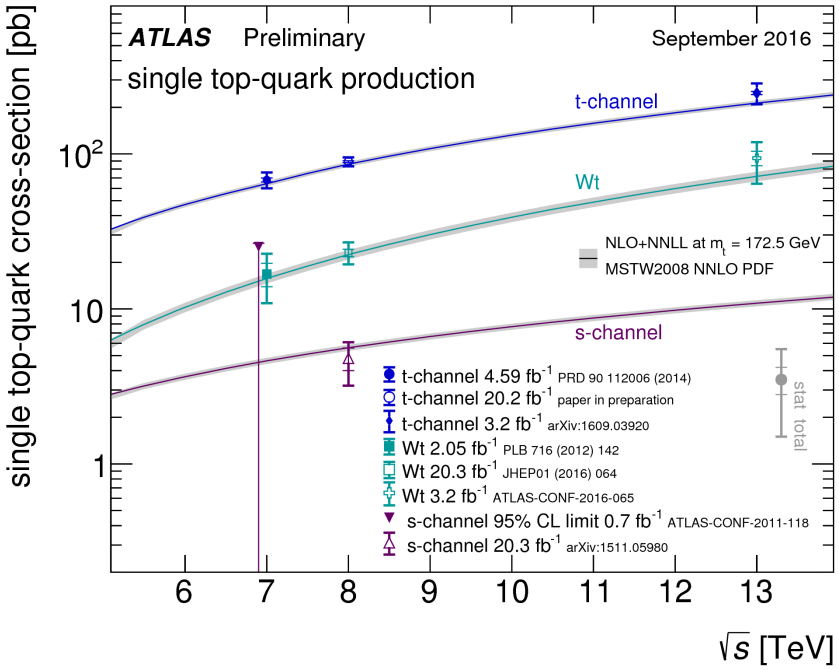

FIGURE 2.6: Single top-quark inclusive cross-section measurements of the ATLAS collaboration compared to theory calculations as functions of centre-of-mass energy . Predictions are based on Hathor 2.1 in NLO+NLL QCD precision.
source: [34]

3. Theoretically predicted cross-section with Hathor

This work is based on a program that performs the indirect top-quark mass measurement and therefore caches, fits and analyses cross-section results obtained using the programs Hathor v2.1 [42] and LHAPDF6.1.6 [43]. The own implementation is labelled xHathor in order to distinguish from Hathor and clearly signalise where own and where included algorithms are referenced. Appendix B describes the installation of the xHathor program and outlines exemplary usage.

Hathor allows for the calculation of inclusive top-quark pair-production cross-sections and single top-quark cross-sections in the three production channels with regard to different sets of parton density functions (PDFs), a reference top-quark mass and beam energy. The implementation at NLO follows [44] for t-channel and s-channel production and [45] for associated tW production. Approximate aNNLO results have been added for t-channel and s-channel theory and are subject to ongoing research and development.

The perturbative expansion of the partonic cross-sections $\hat{\sigma}_{ij}$ in powers of α_s as described by equation 3.1 is possible at high energies, where the quarks can be treated as free particles. This is a consequence of the decreasing of the QCD coupling with the energy scale that is known as asymptotic freedom. Vice versa, due to the increasing coupling strength that leads to confinement at longer distance, quarks in the initial state within the colliding hadrons as well as in the final state have to be treated as bound states and cross-sections cannot be computed in perturbation theory.

$$\hat{\sigma}_{ij}(\hat{s};\mu_r,\mu_f) = \hat{\sigma}_{ij}^{\mathrm{LO}}(\hat{s}) + \alpha_s\hat{\sigma}_{ij}^{\mathrm{NLO}}(\hat{s};\mu_r,\mu_f) + \alpha_s^2\hat{\sigma}_{ij}^{\mathrm{NNLO}}(\hat{s};\mu_r,\mu_f) + \mathcal{O}(\alpha_s^3) \quad (3.1)$$

The dependence on the renormalisation and factorisation scales μ_r and μ_f is detailed in section 3.1. The inclusive cross-section at particle level is given by the summation of the corresponding partonic cross-sections convolved with the parton density functions according to the factorisation theorem that is given in equation 3.2.

$$\sigma(s) = \sum_{i,j}\int\int dx_1 dx_2 f_i(x_1;\mu_f) f_j(x_2;\mu_f)\hat{\sigma}_{ij}(x_1x_2s,\mu_f,\alpha_s(\mu_r)) \quad (3.2)$$

PDFs are sensitive to the underlying model of the process-independent momentum structure of the partons within the proton. They describe the probability densities $f(x_{1,2},\mu_f)$ that a parton $i,j \in \{q,\bar{q},g\}$ carries a momentum fraction between x and $x+dx$ of the proton momentum $p_{1,2}$. In

contrast to the centre-of-mass energy s of the proton-proton system, the energy of the hard scattering $\hat{s} = x_1 x_2 s = x_1 x_2 (p_1 + p_2)^2$ remains unknown. In order to solve equation 3.2, Hathor performs a two-dimensional Monte Carlo integration over the impulse fractions $x_{1,2}$ of the partons using the VEGAS algorithm [46, 47]. Several tools and frameworks have been developed to deploy known theory in the determination of inclusive and differential partonic cross-sections. This analysis typically involves numerical phase space integrations that are particularly cpu-intensive. Hathor follows a different approach using hard coded partonic cross-sections in order to avoid the phase space integration.

In contrast to top-quark pair-production where inclusive partonic cross-section formulae are known, partonic cross-sections for single top-quark production are theorised fully differential. Hathor relies on the implementation present with the MCFM program [48]. Feynman rules are derived from the QCD Lagrangian and are used to calculate matrix elements that are combined with the phase space of the outgoing partons to calculate leading order partonic cross-sections in a five flavour scheme. Next-to-leading order contributions of virtual corrections and real emissions are implemented following the dipole subtraction method to cancel diverging integrals. Lower quark masses are set to zero and the top-quark decay to lower generations is neglected according to $|V_{tb}| = 1$.

Hathor stores partonic cross-section results $\hat{\sigma}_{ij}^{\mathrm{NLO}}(\sqrt{\hat{s}}, m_t)$ that have been extracted from MCFM for 18 top-quark mass points, including very high values of up to almost $1\,\mathrm{TeV}$. A set of 64 points for $\sqrt{\hat{s}}$ is sampled for each mass value, omitting energies below the production threshold $M = m_t$ in the s and t-channel and $M = m_t + m_W$ for tW-production. Forerun computations of the underlying grids for all three production channels have taken a runtime of $\mathcal{O}(10^4)$ hours on the LHC Computing Grid [49]. Leading-order partonic cross-sections are analytically known and computed at runtime.

3.1 Scale uncertainties

The running of the top-quark mass, which is taken into account by the application of the $\overline{MS}$ scheme, and the running of the QCD coupling strength introduce a scale dependency to the obtained results. For the referenced cross-section the renormalisation and factorisation scales are set to $\mu_r = \mu_f = m_t$. The Hathor documentation [42] contains contour plots, arranged in figure 5, that show the two-dimensional cross-section dependence on the two scales and exhibit a significant difference between the production channels. The examination of scale variations in a window $\mu_r = a_r \cdot m_t, \mu_f = a_f \cdot m_t$ limited by $0.5 \leq a_r, a_f \leq 2$ reveals that the t-channel and the tW-production depend much more on μ_f than on μ_r, which leads to higher cross-sections for the upper factorisation scale variation and vice versa. In contrast, for s-channel results, the conclusion is less clear with intermingling anti-correlated effects from both scales. The scale variation reduces significantly with higher order calculations and is used to analyse the dependence of the result on the truncation of the perturbative series.

Scale uncertainties within this work are estimated from two additional evaluations with updated scale settings $\mu_r = \mu_f = a \cdot m_t$ using $a \in (0.5, 2)$ as described by equations 3.3 and 3.4. It is important not to translate upper

and lower scale variation directly to upper and lower uncertainty on the cross-section. For t-channel and tW-production, it holds that the upper scale variation $\mu_r = \mu_f = 2 \cdot m_t$ leads to increasing results and lower scales $\mu_r = \mu_f = 0.5 \cdot m_t$ lead to decreasing results, However, this is not true for the s-channel, where the upper scale variation introduces a lower uncertainty and lower scales result in upper uncertainties on the cross-section.

Within the context of the indirect top-quark mass extraction carried out in chapter 4, the two variations are combined by taking the envelope. The symmetrised value is included into the total uncertainty on the predicted cross-section as described in equation 3.5.

$$\Delta^{\text{up}}_{\text{scale}} = \sigma(\mu_r = \mu_f = 2 \cdot m_t) - \sigma(\mu_r = \mu_f = m_t) \tag{3.3}$$

$$\Delta^{\text{down}}_{\text{scale}} = \sigma(\mu_r = \mu_f = 0.5 \cdot m_t) - \sigma(\mu_r = \mu_f = m_t) \tag{3.4}$$

$$\Delta_{\text{scale}} = \max\left(|\Delta^{\text{up}}_{\text{scale}}|, |\Delta^{\text{down}}_{\text{scale}}|\right) \tag{3.5}$$

This strategy partly follows recommendations of the ATLAS and CMS collaborations [50], but dispenses with four additional variations that would attribute the same values independently by fixing one of the scales to m_t, while doubling and halving the other. This is done in order to facilitate programming and to reduce runtime. This work focusses on the indirect mass measurement carried out in the t-channel and it has been preconceived that the strongest variations in this channel are observed when the scales are changed in equal measure. However, in the s-channel this naive approach tends to slightly underestimate the scale uncertainty. In all cases, the difference between the strategy using the uniform and the independent variation is smaller than $\mathcal{O}(1\,\text{GeV})$.

3.2 PDF uncertainties

PDF modelling is an important prerequisite for cross-section measurements. Parameters are not directly deduced from theory, but determined by fitting data from deep inelastic scattering experiments. Hathor makes use of LHAPDF6, which gives access to a range of PDF fits published by various workgroups[1]. In fact, most of the runtime consumed by Hathor is spent to execute code blocks of LHAPDF6 [49]. By default, the recommended PDF4LHC15_nlo_30_pdfas set [51] is used in the xHathor program. This set updates former recommendations [52] and involves results of three older sets CT14 [53], MMHT2014 [54] and NNPDF3.0 [55]. However, the xHathor implementation can be used with any PDF set that is compatible with the included version of LHAPDF6. Note that sets may use different quark masses and different values of α_s. Furthermore, the strategies for higher order corrections, parametrisation form, systematic uncertainties and confidence level estimations may vary.

With ongoing studies that extend the order of the perturbative series computation, the scale dependence will decrease further and the dependence on the PDF will be the most contributing source of uncertainty. It is

[1] For available PDFs see `https://www.hepforge.org/archive/lhapdf/pdfsets/current`

estimated with respect to the underlying PDF type, which is either symmetric or asymmetric Hessian or equiprobable MC replicas. For all three types the method of error computation described here is the one implemented with the `PDFSet::uncertainty` function in the LHAPDF code that was written following [56].

Replica sets like the PDF4LHC15_nlo_mc with N_{mem} = 100 member PDFs use mean and standard variation for error estimation. The result from the first set is expected to satisfy $F_0 \approx \langle F \rangle$. However, the implementation in LHAPDF evaluates the mean based on the entire set as given in equation 3.6 and 3.7. This matches with the PDF4LHC15 recommendations [51].

$$\langle F \rangle = \frac{1}{N_{\text{mem}}} \sum_{k=1}^{N_{\text{mem}}} F_k \tag{3.6}$$

$$\Delta_{\text{pdf}} = \sqrt{\frac{1}{N_{\text{mem}} - 1} \sum_{k=1}^{N_{\text{mem}}} (F_k - \langle F \rangle)^2} \tag{3.7}$$

The additional requirement to evaluate each member PDF makes the computation of the PDF uncertainty a crucial part of cross-section calculations with regard to runtime.

In the Hessian approach, errors on the fitted data points are propagated by diagonalising the Hessian matrix, that is the $n_{\text{eig}} \times n_{\text{eig}}$ covariance matrix of ordered eigenvectors. The central PDF F_0 is taken as the best fit and the following members represent fits based on variations of the respective eigenvector. For symmetric Hessian sets equation 3.8 explains how the PDF uncertainty is estimated by summation over the contributed deviations. As with replica sets, all additional fits have to be evaluated separately. The defaulted PDF4LHC15_nlo_30 is a symmetric Hessian PDF set that contains variations for 30 eigenvectors. An even more accurate set is available with the PDF4LHC15_nlo_100.

$$\Delta_{\text{pdf}} = \sqrt{\sum_{k=1}^{n_{\text{eig}}} (F_k - F_0)^2} \tag{3.8}$$

Asymmetric Hessian sets contain PDFs for lower and upper uncertainties on the eigenvectors that are propagated to $\Delta^{\pm}_{\text{pfd}}$ as the envelope according to equations 3.9 and 3.10. Within this work, the upper and lower result will be symmetrised equivalent to the scale uncertainty by taking the envelope again as described by equation 3.11.

$$\Delta^{+}_{\text{pdf}} = \sqrt{\sum_{k=1}^{n_{\text{eig}}} \left(\max\{F^{+}_k - F_0, F^{-}_k - F_0, 0\}\right)^2} \tag{3.9}$$

$$\Delta^{-}_{\text{pdf}} = \sqrt{\sum_{k=1}^{n_{\text{eig}}} \left(\max\{F_0 - F^{+}_k, F_0 - F^{-}_k, 0\}\right)^2} \tag{3.10}$$

$$\Delta_{\text{pdf}} = \max\left(|\Delta^{+}_{\text{pdf}}|, |\Delta^{-}_{\text{pdf}}|\right) \tag{3.11}$$

Starting from version 6.1.6 LHAPDF supports combined PDF sets that include the estimation of uncertainties introduced via the QCD coupling constant α_s or other parameters. While the first n_{eig} members are used for a PDF uncertainty estimation as described above, in combined sets additionally the last n_{par} PDFs are produced using parameter variations. The uncertainty is extracted from LHAPDF6 as combined value $\Delta_{\text{pdf},\alpha_s}$. For sets that do not include the respective PDFs, the contribution resulting from the variation of α_s is neglected. For the default set PDF4LHC15_nlo_30_pdfas the naming scheme exhibits that it does contain the α_s parameter variations. At the 68% confidence level the used central value and the associated uncertainty are set to $\alpha_s(M_Z^2) = 0.1180 \pm 0.0015$.

The Hathor code used for this thesis was patched to make this new feature accessible by adding a function that returns the instance of LHAPDF6 constructed by Hathor. A command line switch was added to xHathor in order to leave the user the choice whether to use the respective function from Hathor or from LHAPDF6. Throughout this work the latter is used. Notably, LHAPDF6 processes the PDF type from the set information to determine how to estimate the PDF uncertainty. In the Hathor program, this is conditioned by the PDF name and in parts by relying on the user to pass the `PDF_SYM_ERR` flag, which is prone to false usage. The automatised procedure in Hathor does not correctly resolve PDF4LHC15 sets based on their name. Thus, in absence of the user set flag, the PDF uncertainty estimation produces wrong results. The xHathor program determines the PDF type equivalent to the LHAPDF6 method and handles the user setting correctly. More detailed documentation of the changes made to the Hathor implementation is included in appendix B.

3.3 Hathor results within total uncertainty

Uncertainties that vanish with higher precision of the numerical integration can be neglected and are not included in the total uncertainty that is defined in 3.12. Results shown in this work have been calculated using xHathor at highest precision where $|\sigma_2 - \sigma_1| < 10^{-5}$ holds for any two calculations that share the same settings. Running the integration with lower accuracy reduces the runtime significantly. Even with medium (10^{-4}) and low (10^{-3}) accuracy the uncertainties of this class are much smaller compared to the scale and to PDF+α_s uncertainties.

$$\Delta\sigma = \Delta_{\text{total}} = \sqrt{\Delta^2_{\text{scale}} + \Delta^2_{\text{pdf}} + \Delta^2_{\alpha_s}} \tag{3.12}$$

Hathor cross-section results and uncertainties on a $68\,\%$ certainty level are shown in table 3.1 for a reference top-quark mass of $172.5\,\text{GeV}$ using the PDF4LHC_nlo_30_pdfas set. The usage of the PDF4LHC_nlo_30 set would give almost equal results within the numerical uncertainty, but would neglect the comparably small contribution of the α_s uncertainty, consequently yielding a slightly smaller estimation of the total uncertainty.

The accuracy is better in the t-channel and the s-channel, whereas the larger uncertainty in the tW-channel is mainly introduced by the PDF+α_s error estimation. The sign change in the upper and lower scale uncertainty

in the s-channel recalls its specific scale dependence, which would be estimated by up to $\mathcal{O}(1\,\mathrm{GeV})$ larger when following PDF4LHC15 recommendations more strictly.

channel	$\sigma[pb]$	$\Delta_{\text{total}}[\%]$	$\Delta^{\text{down}}_{\text{scale}}[\%]$	$\Delta^{\text{up}}_{\text{scale}}[\%]$	$\Delta_{\text{scale}}[\%]$	$\Delta_{\text{pdf}}[\%]$	$\Delta_{\alpha_s}[\%]$
tq	55.61 ± 2.33	4.2	-1.7	2.9	2.9	2.7	1.3
$\bar{t}q$	30.28 ± 1.50	5.0	-1.6	3.0	3.0	3.6	1.6
$tq + \bar{t}q$	85.89 ± 3.77	4.4	-1.6	2.9	2.9	2.9	1.4
$t\bar{b}$	3.33 ± 0.10	3.0	2.3	-1.7	2.3	1.9	0.8
$\bar{t}b$	1.90 ± 0.06	3.1	2.2	-1.7	2.2	2.1	0.8
$t\bar{b} + \bar{t}b$	5.22 ± 0.15	3.0	2.2	-1.7	2.2	1.9	0.8
tW	9.04 ± 0.70	7.8	-4.2	2.4	4.2	5.9	2.7
$\bar{t}W$	9.03 ± 0.70	7.8	-4.2	2.5	4.2	5.9	2.7
$tW + \bar{t}W$	18.08 ± 1.40	7.8	-4.2	2.4	4.2	5.9	2.7

TABLE 3.1: Hathor cross-section results for the PDF4LHC sets with 30 eigenvectors. The cross-sections are shown together with the absolute uncertainty in picobarn, which is also given as relative uncertainty.

3.4 Dependence on the top-quark mass

Theoretical predictions for top-quark cross-sections monotonically decrease with the assumed top-quark mass regardless of the production process. The curves for all three single top-quark production channels and for $t\bar{t}$-production are drawn for $8\,\mathrm{TeV}$ pp-collisions in figure 3.1. Their slopes exhibit significant differences that are formally described in this section. The t-channel has the lowest mass dependence and the highest cross-sections of all production processes in the domain of masses heavier than roughly $250\,\mathrm{GeV}$. The grids implemented in the Hathor program cover a range between $165\,\mathrm{GeV}$ and $950\,\mathrm{GeV}$. The upper limit reflects the domain where t-channel results stay larger than roughly $1\,\mathrm{pb}$ at the energy of $8\,\mathrm{TeV}$ and larger than roughly $10\,\mathrm{pb}$ at the energy of $14\,\mathrm{TeV}$. In contrast, s-channel cross-sections and associated tW-production and also $t\bar{t}$-production have negligible cross-section predictions for much lighter limits. The strongest mass dependence is observed for top-quark-antiquark pair-production. This can be compared in the in-set in figure 3.1 on a non-logarithmic scale, normalised to the respective results at the reference top-quark mass and zoomed to a small interval around this mass. In this window, all curves appear to be almost linear. For higher centre-of-mass energies (not drawn here) the cross-sections increase while the observed mass dependencies slightly decrease.

For all three single top-quark production processes the theoretical results match very well with the parametrisation given in equation 3.13 that has also been applied to model the mass dependence of $t\bar{t}$ cross-sections [57]. For the following analysis it is used to fit Hathor results in the interval

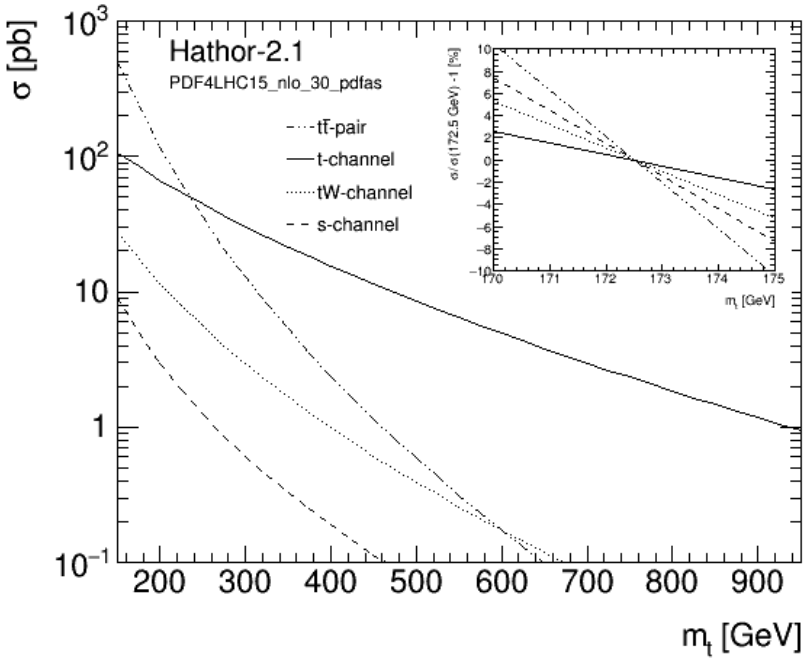

FIGURE 3.1: Cross-sections at $8\,\mathrm{TeV}$ calculated using Hathor 2.1 and fitted to equation 3.13. The grey band shows the symmetric PDF error calculated by LHAPDF6.1.6

$172.5 \pm 12.5\,\mathrm{GeV}$ that are sampled with a step width of $1.25\,\mathrm{GeV}$.

$$\sigma(m_t) = \sigma(m_{\mathrm{ref}}) \left(\frac{m_{\mathrm{ref}}}{m_t}\right)^4 \left[1 + a_1 \left(\frac{m_t - m_{\mathrm{ref}}}{m_{\mathrm{ref}}}\right) + a_2 \left(\frac{m_t - m_{\mathrm{ref}}}{m_{\mathrm{ref}}}\right)^2\right] \quad (3.13)$$

When masses below $160\,\mathrm{GeV}$ and above $185\,\mathrm{GeV}$ are used to perform the indirect top-quark mass extraction in this work, cross-sections are extrapolated by evaluation of the respective fit result.

The obtained fits for the central results and for the scale variations are presented in figure 3.2 alongside the PDF uncertainty. This plot illustrates all data that is actually extracted from the Hathor program. In the t-channel, the fit for the upper scale variation coincides well with the symmetric PDF uncertainty, whereas the lower uncertainty is dominated by the PDF error. The total uncertainty that has been defined in equation 3.12 is drawn as grey error band in figure 3.3. Fits based on equation 3.13 match the total uncertainty as depicted by the dotted lines and the extracted cross-sections as shown by the continuous line.

The mass-dependence δ of the theory calculations is deduced from the fit function by evaluation of the derivative at the reference top-quark mass as defined in equation 3.14. Cross-sections may differ by several orders of magnitude, hence the relative mass dependence $\bar{\delta}$ as defined in equation 3.15 is used to compare the mass dependence between different processes and collision energies.

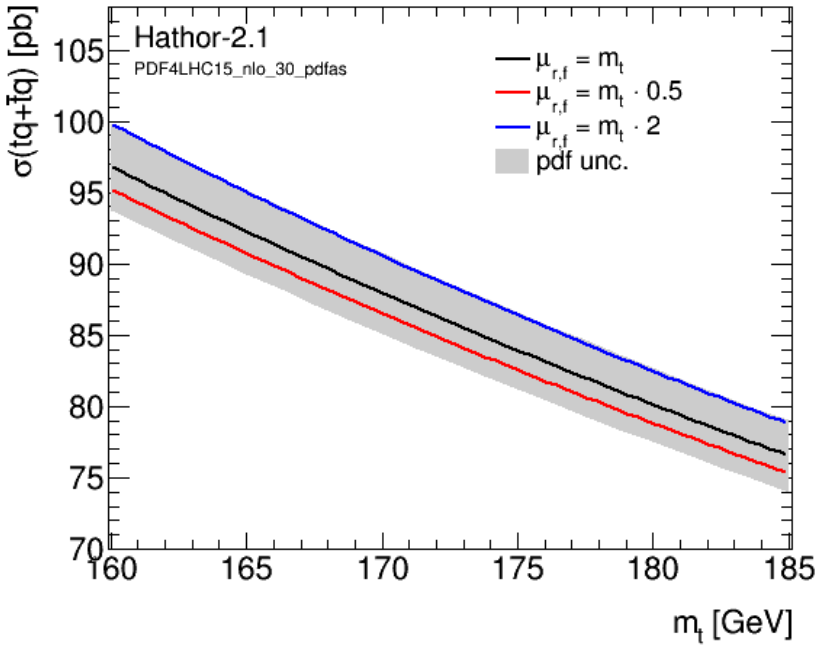

FIGURE 3.2: Continuous lines show the combined t-channel cross-sections at $8\,\mathrm{TeV}$ for the central result $\mu_r = \mu_f = m_t$ and for the upper and lower scale uncertainty. Hathor results are taken with a step width of $1.25\,\mathrm{GeV}$ and fitted to equation 3.13. The gray band shows the symmetric PDF error extracted from LHAPDF6.1.6.

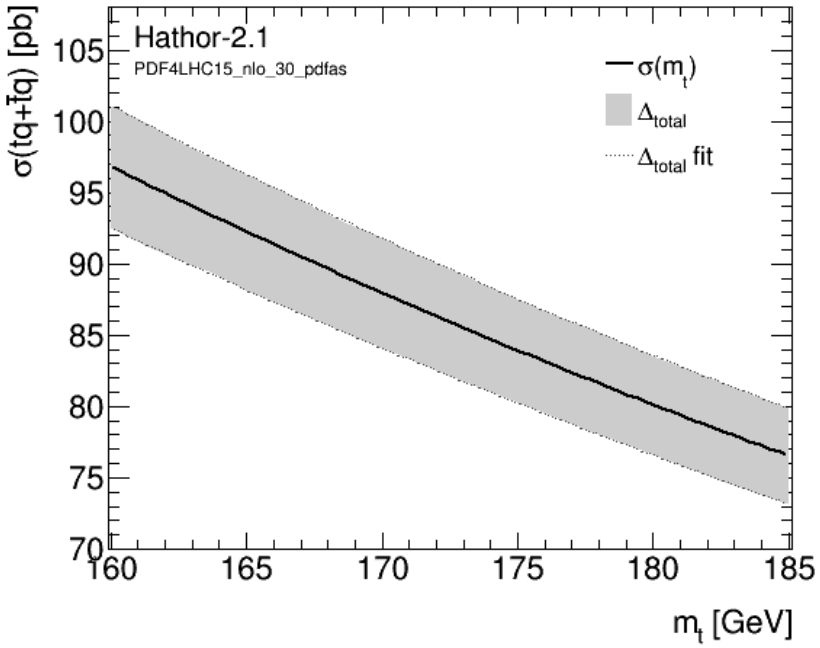

FIGURE 3.3: The continuous line shows the combined t-channel cross-section at $8\,\mathrm{TeV}$ for the central result $\mu_r = \mu_f = m_t$ fitted to equation 3.13. The grey band shows the combined scale+PDF+α_s uncertainty. The dotted lines show the fit results that are used to extrapolate uncertainties.

$$\delta = \frac{d\sigma(m_t)}{dm_t}(m_{\text{ref}}) \quad \left[\frac{\text{pb}}{\text{GeV}}\right] \tag{3.14}$$

$$\bar{\delta} = 100 \cdot \frac{\delta}{\sigma(m_{\text{ref}})} \quad \left[\frac{\%}{\text{GeV}}\right] \tag{3.15}$$

The fit parameters for equation 3.13 are given in table 3.2 where the central cross-section at the reference top-quark mass is evaluated from the fit result. Within the same channel there is no significant difference between the mass dependence of top-quarks and top-antiquarks. The t-channel shows the largest absolute mass dependence with $-0.81\,\frac{\text{pb}}{\text{GeV}}$. As a consequence, combined t-channel cross-sections vary about $10\,\text{pb}$ in the evaluated interval that has a width of $\pm 12.5\,\text{GeV}$. At the same time, the relative mass dependence is the lowest in the t-channel with less than $1\,\frac{\%}{\text{GeV}}$. The strongest relative mass dependence is observed in the s-channel that in turn has the lowest cross-sections.

channel	$\sigma(m_{\text{ref}})[pb]$	a_1	a_2	$\delta\left[\frac{\text{pb}}{\text{GeV}}\right]$	$\bar{\delta}\left[\frac{\%}{\text{GeV}}\right]$
tq	55.61	2.408	1.286	-0.51	-0.9
$\bar{t}q$	30.28	2.328	1.171	-0.29	-1.0
$tq + \bar{t}q$	85.89	2.376	1.218	-0.81	-0.9
$t\bar{b}$	3.33	0.205	-0.017	-0.07	-2.2
$\bar{t}b$	1.90	0.005	0.038	-0.04	-2.3
$t\bar{b} + \bar{t}b$	5.22	0.120	0.003	-0.12	-2.2
tW	9.04	1.021	-0.552	-0.16	-1.7
$\bar{t}W$	9.03	1.021	-0.553	-0.16	-1.7
$tW + \bar{t}W$	18.08	1.021	-0.552	-0.31	-1.7

TABLE 3.2: Fit parameters according to equation 3.13 for Hathor cross-sections using the PDF4LHC_nlo_30_pdfas set in $8\,\text{TeV}$ pp-collisions. The absolute and relative mass dependence according to equations 3.14 and 3.15 as well as the listed cross-section are obtained from the fit result.

In addition to equation 3.13, the applicability of polynomial fitting was examined with a linear and a quadratic function, both fixed to $\sigma(m_{\text{ref}})$ similar to the default fit function. The overlay in figure 3.4 demonstrates that the mass dependence is close to linear in the shown interval $172.5 \pm 20\,\text{GeV}$ that contains the region of interest for the top-quark mass measurement. Within this region, the error made by using a linearisation is limited by approximately $2\,\text{pb}$, which is smaller than the given total uncertainty and even smaller than the scale and PDF uncertainties. The quadratic polynomial is completely covered by the overlaying red graph that shows the extrapolation according to equation 3.13. This coverage is enhanced by the low mass dependence of the t-channel. For the other channels the curves are more distinct. The respective figures can be found in appendix A. For combined t-channel results the fit quality measured by means of χ^2/NDF is not sufficient for a linear model, while it amounts to 2.3 for the quadratic function

and to 0.9 for the default parametrisation. The extrapolation shows that the applicability of linear and quadratic functions is limited to a region close to the interpolation interval. For higher particle masses the linear function yields negative results, while the quadratic polynomial yields again increasing cross-sections. The usage of higher polynomials would exhibit further unfavourable unphysical curves in the extrapolation region.

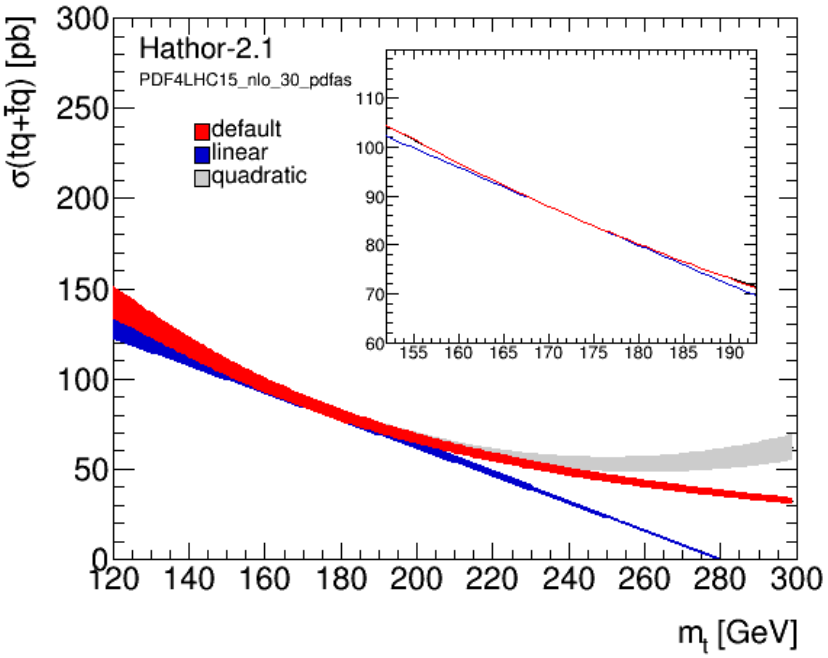

FIGURE 3.4: Extrapolation based on different models using Hathor cross-section results taken with a step width of $1.25\,\mathrm{GeV}$ in the interval $160 - 185\,\mathrm{GeV}$. The filled areas indicate the extrapolated total uncertainty based on the combined scale+PDF+α_s error. The overlay shows the fits for the central results without uncertainties.

4. Extraction of the top-quark pole mass

The discussed fits of the theoretically constructed expectations can be used to map top-quark masses given in the pole mass scheme to cross-section predictions. The inverse mapping allows to interpret experimentally obtained cross-section results as measurements of the pole mass. Obviously, the precision is limited by the experimental and theoretical uncertainties, but the dominant factor for the accuracy of such an indirect mass measurement is the difference between the mass dependence of the experimental and theoretical results. The realised experiments at the LHC and the Tevatron produced results that depend on the top-quark mass as an input parameter, which is expectable from the outstanding role of the top-quark mass within the Standard Model. In fact, there is no demand that experimental and theoretical results match for arbitrary virtual top-quark masses as input parameter for MC generators. The agreement between experiment and theory is required only for the natural top-quark mass as a parameter of the Standard Model.

The cross-section measurements by methods of direct reconstruction use Monte Carlo generators to simulate particle collisions within a simulated detector environment. These generators model the running of the top-quark mass m_t^{MC} in the $\overline{MS}$-scheme that consequently has to be translated into the pole mass scheme, in which the values obtained from the Hathor program are fixed. The estimated uncertainty of the conversion between the different mass models has been shown to compare with $\mathcal{O}(\Lambda_{\mathrm{QCD}})$. The remainder of the series expansion of the mass conversion factor from terms above the four-loop order is smaller than $250\,\mathrm{MeV}$ and the uncertainty propagated from included parameters is smaller than $70\,\mathrm{MeV}$, which compares to the intrinsic limitation of the accuracy of the pole mass scheme [1]. Facing discussed uncertainties that are considerably larger than these estimations the $\overline{MS}$ mass can be directly used in the pole mass scheme. Uncertainties of the mass scheme conversion cancel naturally when the dependence of the measured cross-section on the MC mass vanishes.

4.1 Applicability and expected precision

The difference between the mass dependencies can be related to the crossing angle of the curves that represent the expected and observed cross-sections. This is sketched in figure 4.1 for an idealised experimental outcome that is independent of the top-quark mass and has negligible uncertainties. In this simplified case, the difference between the mass dependencies is given by the mass dependence of the theoretical results and can be read directly from table 3.2.

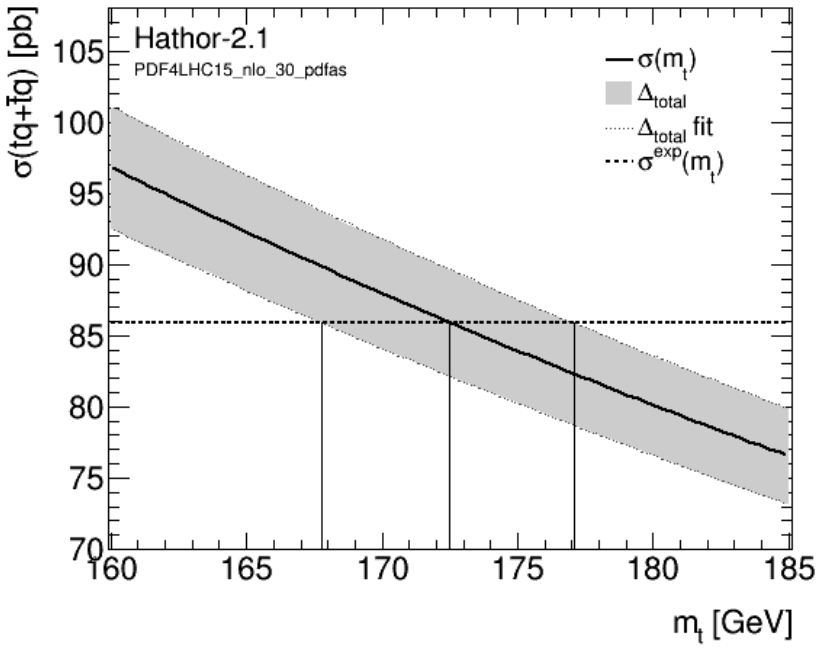

FIGURE 4.1: The intersection of a constant curve corresponding to a mass independent measurement technique at the central value of the predicted cross-section of $85.89\,\mathrm{pb}$. The extracted top-quark mass is $172.5^{+4.6(2.6\%)}_{-4.7(2.7\%)}\,\mathrm{GeV}$.

The measured cross-section is modelled by a linear function according to equation 4.1. The extracted top-quark pole mass is determined at the intersection point between this curve and the central fit of the theoretical result. In the simplified plot, the experimental cross-section is fixed to the expectation value. As a consequence, the intersection is located exactly at the reference top-quark mass. The upper and lower uncertainties of the measurement are evaluated by intersecting the experimental curve with the fits through the total uncertainties, which enclose the grey error-band.

$$\sigma^{\mathrm{exp}}(m_t) = \sigma^{\mathrm{exp}}(m_{\mathrm{ref}}) + \frac{d\sigma^{\mathrm{exp}}}{dm_t}(m_t - m_{\mathrm{ref}}) \tag{4.1}$$

A reduced difference in mass dependence leads to more parallel graphs and therefore to less accuracy of the assessed top-quark mass, since these intersections move away from the centre point. For an experimental result that perfectly matches the Hathor predictions along the pole mass axis, the method breaks down completely. Following this argument, the optimal precision can be achieved for an experimental outcome, which tangents the normal in the intersection point and maximises the difference in mass dependence.

Given an experimental result and its mass dependence, the expectable precision of an indirect mass measurement can be estimated from figure 4.2. The possible experimental mass dependencies are drawn along the x-axis and the pole that divides the plot into a right and left side corresponds to the $-0.81\,\frac{\mathrm{pb}}{\mathrm{GeV}}$ mass dependence of the Hathor predictions. This pole resides in the negative domain of the x-axis, because theoretical cross-section predictions have strictly negative derivatives. All mass dependencies left

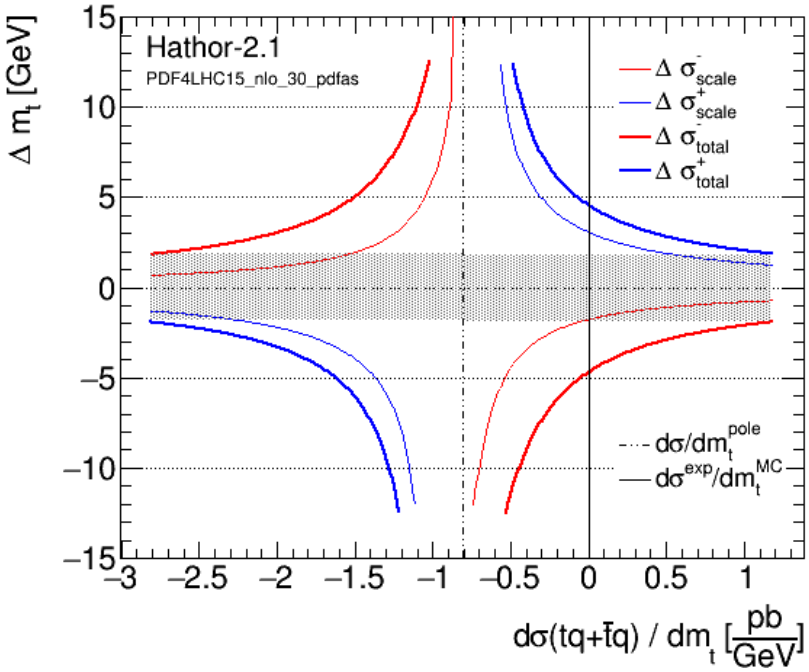

FIGURE 4.2: Achievable precision of an indirect top-quark mass measurement for varying mass dependence of the experimental cross-section. The blue and red lines show the implications of the total uncertainties (bold) and the scale uncertainty (fine) of the Hathor result. The continuous vertical line marks a mass independent experiment that yields $-4.7\,\mathrm{GeV}$ $(-2.7\,\%)$ lower and $+4.6\,\mathrm{GeV}$ $(2.6\,\%)$ upper uncertainty. The horizontal filled area illustrates the accuracy for orthogonal mass dependencies that evaluates to $-1.9\,\mathrm{GeV}$ $(-1.1\,\%)$ lower and $+1.8\,\mathrm{GeV}$ $(1.0\,\%)$ upper uncertainty.

of the pole stand for experimental curves that intersect the theory curve from above and that have an even higher negative derivative at the intersection point. Likewise, all mass dependencies right of the pole stand for experimental curves that intersect the theory curve from below. In figure 4.1 it can be verified that in the latter case, especially for mass independent measurements, the lower uncertainty on the theoretical results translates into the lower uncertainty on the top-quark mass and on the other side the upper uncertainty on the theoretical results translates into the upper uncertainty on the top-quark mass. This is alternated when the curve that represents the experimental results intersects the theory curve from above. In figure 4.2 this leads to the alternation of the red and blue lines that both demarcate the expected accuracy of the top-quark mass measurement and that change the sign at the pole. The grey band shows the optimal accuracy that can be achieved by an orthogonal intersection of the two curves drawn in figure 4.1, which occurs for an experimental mass dependence of $1.23\,\frac{\mathrm{pb}}{\mathrm{GeV}}$. This corresponds to a relative mass dependence of $(1.4\,\frac{\%}{\mathrm{GeV}})$ and yields a result for the top-quark mass with approximately $1\,\%$ precision that is $172.5^{+1.8(1.0\%)}_{-1.9(1.1\%)}\,\mathrm{GeV}$. For a mass independent measurement, which is indicated by the vertical continuous line, the achievable precision is estimated

to be $172.5^{+4.6(2.6\%)}_{-4.7(2.7\%)}$ GeV.

4.2 Implemented maximum likelihood method

A considerable number of repetitions of the Hathor calculations is expected to yield a Gaussian distribution in each mass bin that is described by equation 4.2. The mean $\sigma^{\text{th}}(m_t)$ corresponds to equation 3.13 and the standard deviation $\Delta^{\text{th}}_{\text{total}}(m_t)$ to equation 3.12. As discussed, mean and standard deviation both depend on the top-quark pole mass. When restricted to a width of plus/minus one standard deviation, the result for an interval on the pole mass axis can be expected to reproduce the graph in figure 3.3 that illustrates the theoretical prediction.

$$f(\sigma; m_t, \sigma, \Delta_{\text{total}}) = \frac{1}{\sqrt{2\pi}\Delta_{\text{total}}} e^{-\frac{1}{2}\left(\frac{\sigma-\langle\sigma\rangle}{\Delta_{\text{total}}}\right)^2} \tag{4.2}$$

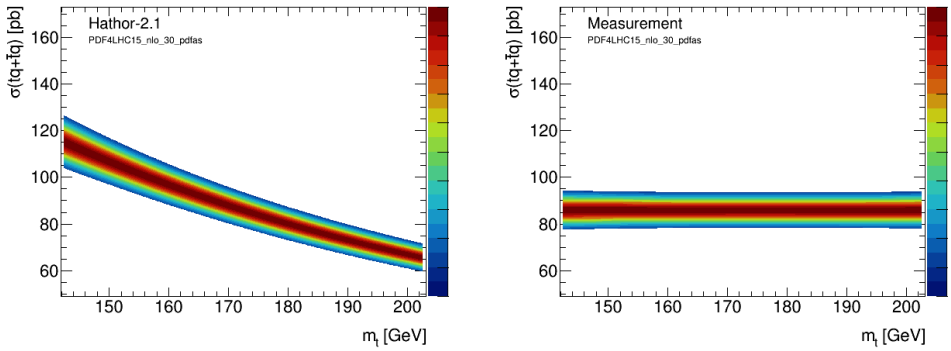

(a) Mean and standard deviation of the theory predictions are extrapolated according to equation 3.13.

(b) Mean and standard deviation of the experimental result are set to the Hathor cross-section and uncertainty for $m_t = 172.5\,\text{GeV}$.

FIGURE 4.3: Simulated pseudo experiments with Gaussian distributions in each mass bin according to equation 4.2. Both histograms are sampled with 1000×1000 cross-section values that stand for repetitions of the theoretical prediction (left) and the experimental measurement (right). For reasons of readability only two standard deviations respectively $95.45\,\%$ of the pseudo experiments are drawn.

Figure 4.3a shows the theoretical distribution sampled with 1000×1000 pseudo experiments and drawn with a width of plus/minus two standard deviation, which covers approximately $95.45\,\%$ simulated repetitions of the Hathor calculations. Figure 4.3b shows the same histogram for the experimental curve, for which the mean is modelled according to equation 4.1. The uncertainty on the experimental distribution is no longer neglected, but set to the $4.4\,\%$ total uncertainty of the theory predictions. The user of the xHathor program can configure the experimental uncertainty, as well as the mean and the slope of the distribution. Here the setting is chosen in order to illustrate the potential of the method for an experimental accuracy that closes up with the theoretical precision.

Given a mass bin i, let L_{ij} be the likelihood that both, a randomly picked pseudo experiment sampling the Hathor values and a second randomly picked pseudo experiment sampling the experimental values, yield a cross-section corresponding to bin j on the cross-section axis. Given the independence of the theoretical predictions and the experiment, L_{ij} equals the product of the respective probabilities, which is stated by equation 4.3. The combined likelihood $L_i = L(m_t)$ for a given top-quark mass is evaluated as the integral along the cross-section axis according to equation 4.4. Then the top-quark pole mass can be assessed by finding the maximum of the combined likelihood distribution along the pole mass axis as defined in equation 4.5.

$$L_{ij} = f(\sigma_j; m_i, \sigma_i^{\text{th}}, \Delta_i^{\text{total}}) \cdot f(\sigma_j; m_i, \sigma_i^{\text{exp}}, \Delta_i^{\text{total}}) \tag{4.3}$$

$$L(m_t) = \int f(\sigma'; \sigma^{\text{th}}(m_t), \Delta_{\text{total}}(m_t)) \cdot f(\sigma'; \sigma^{\text{exp}}(m_t), \Delta_{\text{total}}(m_t)) d\sigma' \tag{4.4}$$

$$m_t^{\text{pole}} = \max_{m_t}(L(m_t)) \tag{4.5}$$

The distribution of the likelihood L_{ij} is shown in figure 4.4. All sampled pseudo experiments from the two histograms drawn in figure 4.3 were involved in the multiplication, including the ones further away than two standard deviations from the mean that were omitted from the plots. Again, the drawn area, which resembles an ellipse, is restricted to two standard deviations by introducing a threshold that corresponds to $95.45\,\%$ of the histogram content. The ellipse diameter is discernibly larger in direction of the mass axis than in direction of the cross-section axis.

From this two dimensional distribution, the projection onto the mass axis is performed in order to evaluate the bin-wise integral defined in equation 4.4. To finally determine the top-quark mass, the marginal that is shown in figure 4.5 is evaluated as follows. The mode, that is the mass bin with the maximum of the likelihood distribution at $172.4\,\text{GeV}$, is taken as the measured result. To deduce the uncertainty the values that embrace the central $66.27\,\%$ of the histogram content are determined and quoted as $m^{0.16}$ and $m^{0.84}$. This yields a lower uncertainty of $-6.5\,\text{GeV}$ ($-3.8\,\%$) and an upper uncertainty of $6.6\,\text{GeV}$ ($3.8\,\%$). Compared to the estimated achievable accuracy that was discussed using figure 4.2, this result has approximately $2\,\text{GeV}$ larger uncertainties. The method underlying the estimation, however, neglected the experimental uncertainty, following the strategy that was sketched in figure 4.1. This can be used for an interpretation that distinguishes between experimental and theoretical sources of uncertainty and to give the extracted top-quark mass as $m_t = 172.4\,^{+4.6(2.6\%)}_{-4.7(2.7\%)}$ (theo.) $^{+4.7(2.7\%)}_{-4.5(2.6\%)}$ (exp.) GeV. Strictly speaking, the quadratic combination of the theoretical and experimental uncertainties relies on the independence of the two, which is in fact diluted by correlating scale and PDF dependencies. Keeping this in mind, the distinction is still interesting to observe: when the difference in mass dependencies is varied, the uncertainty classified as theoretical is affected, and when the uncertainty of the experimentally obtained cross-section is varied, only the uncertainty classified as experimental is affected.

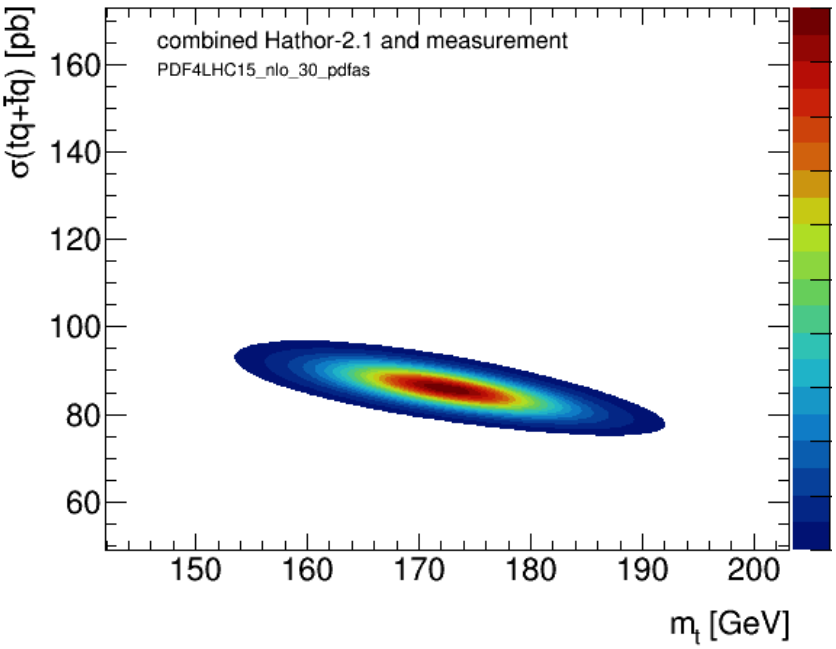

FIGURE 4.4: Likelihood distribution L_{ij} as defined in equation 4.3 obtained by bin-wise multiplication of the two distributions from figure 4.3. A likelihood threshold restricts the drawn area to two standard deviations corresponding to $95.45\,\%$ of the histogram integral.

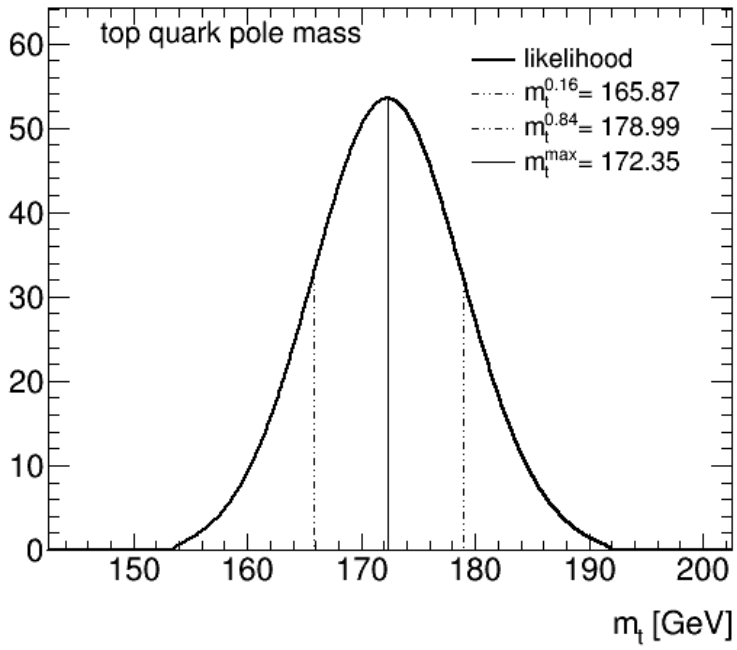

FIGURE 4.5: The result is extracted from the maximum of the likelihood marginal on the mass axis. The dotted lines show $m^{(0.16)}$, $m^{(0.84)}$ that embrace the central $66.27\,\%$ of the histogram content. The measured result is $m_t = 172.4^{+6.6}_{-6.5}\,\mathrm{GeV}$, which reaches an accuracy of $\pm 3.8\,\%$.

5. Experimentally obtained top-quark data

In this chapter a recent measurement of single top-quark t-channel production using $8\,\mathrm{TeV}$ data recorded with the ATLAS detector is summarised and the mass dependence of this measurement is reflected with regard to the discussed indirect top-quark mass extraction. Unless marked otherwise, all results quoted in this chapter refer to [58]. This section provides a short description of the experimental setup.

The LHC collider ring hosts four large detectors ATLAS, CMS, ALICE and LHCb at the four interaction points of the two proton beams. The main collider ring is installed about $100\,\mathrm{m}$ underground in a tunnel with $26.7\,\mathrm{km}$ circumference. The beams are kept in the circuit by a system of 1232 main dipole magnets with field strengths of $8.4\,\mathrm{T}$ at a working temperature below $2\,\mathrm{K}$. A chain of accelerating systems is in place to fill the LHC with about 10^{11} protons per beam, which are grouped to about 1400 bunches per beam. In the $8\,\mathrm{TeV}$ run, the bunch separation was $50\,\mathrm{ns}$, which corresponds to a bunch crossing frequency of $20\,\mathrm{MHz}$. The term event describes a bunch crossing with at least one reconstructed collision. Averaged over the data set, there are about 21 interactions per bunch crossing, which is referred to as pileup.

The observed number of interactions corresponding to a given process is directly proportional to the respective cross-section, as described by equation 5.1.

$$\hat{\nu} = \frac{N_{\text{sel}}}{N_{\text{total}}} \cdot \frac{N_b N_1 N_2 f}{A_{\text{eff}}} \cdot \sigma = \epsilon \cdot \mathcal{L}_{\text{int}} \cdot \sigma \tag{5.1}$$

Given a crossing frequency f and N_b bunches containing N_1 and N_2 particles, the area A_{eff} of the elliptical transverse profile of the interaction region is a key parameter for the achieved integrated luminosity $\mathcal{L}_{\text{int}}$ [59]. The limited event selection efficiency ε leads to a reduced number $N_{\text{sel}} < N_{\text{total}}$ of reconstructed and selected events. A simplified order calculation (neglecting that luminosity decreases with runtime) for the instantaneous luminosity of the LHC $\mathcal{L} = 10^{34}\,\mathrm{cm^{-2}s^{-1}} = 10^{-2}\,\mathrm{pb^{-1}s^{-1}}$ yields that a process with cross-section $\sigma = 1\,\mathrm{pb}$ is produced in average every 100 seconds. The integrated luminosity of the analysed data sample is $\mathcal{L}_{\text{int}} = 20.3\,\mathrm{fb^{-1}}$, recorded between run 200841 on 05.04.2012 and run 215643 on 06.12.2012. [60, 61].

The total number of produced events is not observable, hence the event selection efficiency is obtained from a simulated signal sample. The sum of all event weights is used as N_{total} and N_{sel} is the sum of weights after applying all selection cuts corresponding to the respective cross-section. The event selection efficiency can be decomposed into the reconstruction efficiency and the method dependent fraction A_{fid} of single top-quark events

in the observed phase space. The principle of the fiducial measurement is to determine the cross-section in the so called fiducial volume, which is defined within the detector acceptance close to the phase space of the reconstructed and selected data set. The fiducial acceptance is simulated by the sum of event weights in the fiducial volume N_{fid} as defined in equation 5.2 and used in equation 5.3 to rewrite equation 5.1 to the definition of the inclusive cross-section. This yields the definition of the fiducial cross-section that is given in equation 5.4.

$$A_{\text{fid}} = \frac{N_{\text{fid}}}{N_{\text{total}}} = \frac{\sigma_{\text{fid}}}{\sigma_{\text{inc}}} \tag{5.2}$$

$$\sigma_{\text{inc}} = \frac{1}{\frac{N_{\text{sel}}}{N_{\text{total}}}} \frac{\hat{\nu}}{\mathcal{L}_{\text{int}}} = \frac{1}{\frac{N_{\text{sel}}}{N_{\text{fid}}} \frac{N_{\text{fid}}}{N_{\text{total}}}} \frac{\hat{\nu}}{\mathcal{L}_{\text{int}}} = \frac{1}{A_{\text{fid}}} \frac{N_{\text{fid}}}{N_{\text{sel}}} \frac{\hat{\nu}}{\mathcal{L}_{\text{int}}} \tag{5.3}$$

$$\sigma_{\text{fid}} = \frac{N_{\text{fid}}}{N_{\text{sel}}} \frac{\hat{\nu}}{\mathcal{L}_{\text{int}}} \tag{5.4}$$

Measurements in the fiducial volume benefit from cancelling uncertainties introduced by the Monte Carlo event generators in the extrapolation to the full but not fully accessible phase space of inclusive single top-quark production. The uncertainties that stem from the theoretical aspects, like the pdf modelling and the renormalisation scale, are significantly reduced in the fraction $N_{\text{fid}}/N_{\text{sel}}$ and uncertainties that effect both quantities in the same way cancel completely. Furthermore, this class of methods decouples the cross-section measurement in the fiducial volume and the extrapolation, allowing for a more differentiated and modularised analysis.

5.1 The ATLAS detector

The purpose of the ATLAS detector is to identify particles that are produced in the collisions in the interaction region. Most of these particles and the subsequent decay chains interact with detector parts leading to particle showers, which are reconstructed within cones in the three dimensional detector geometry. Additional particles are produced from initial (ISR) and final state radiation (FSR). Recorded signals, so called hits in detector cells, are analysed and trajectories of particles with a lifetime of at least $3 \cdot 10^{-11}\,\text{s}$ are reconstructed. These tracks are grouped in order to perform jet identification and vertex finding, while avoiding merging pileup vertices.

Figure 5.2 shows a model of the ATLAS detector and its main subdetectors, which are briefly described in the following based on the technical design report [63]. A detailed description and extensive material from a series of notes based on simulations of the ATLAS detector has been published with [64]. A right-handed coordinate system is applied to the cylindrical ATLAS geometry with a barrel and two end-cap sections. The origin lies in the interaction region in the center of the detector and the z-axis points counter clockwise (viewed from above) in direction of the beam line. The x-y plane is transverse to the beam line with the x-axis pointing towards the center of the collider ring and the y-axis pointing upwards. Detector regions are expressed by polar coordinates. The polar angle θ is given with respect to the beam line in the y-z plane and the azimuthal angle

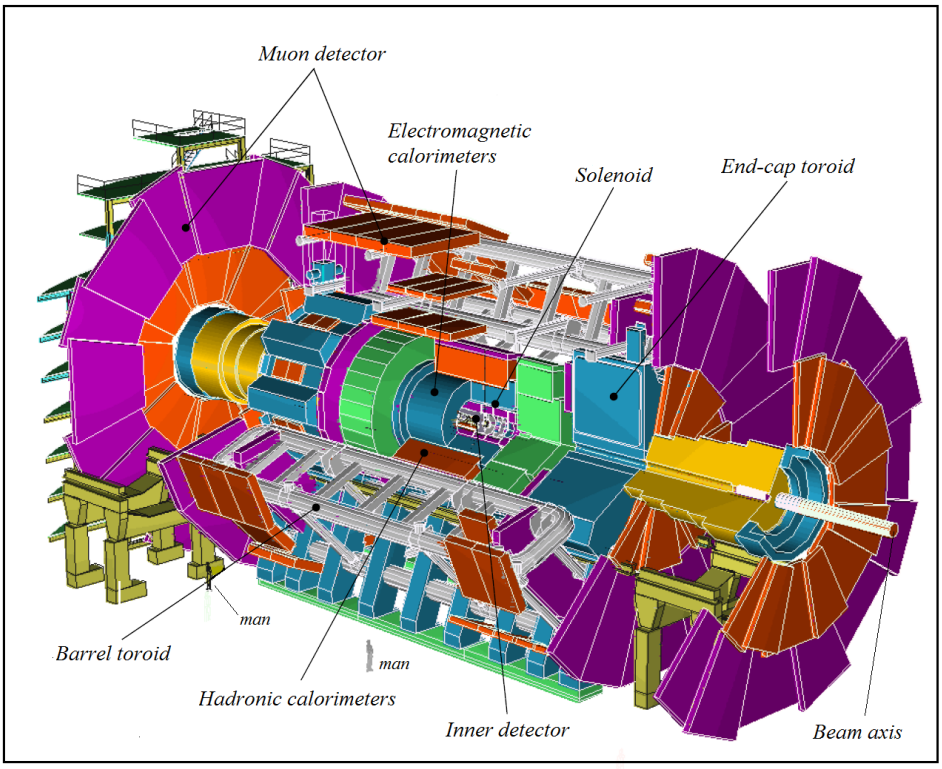

FIGURE 5.1: Model of the ATLAS detector and its main components. Closest to the interaction point lies the inner tracking system that is surrounded by a superconducting solenoid. The outer cylinder and the end-caps host electromagnetic and hadronic calorimeters and a muon spectrometer with three superconducting toroid magnetic systems.
source: [62]

ϕ around the beam line is measured in the transverse plane. The pseudo rapidity η is defined as $\eta = -\ln(\tan(\theta/2))$ and the angular distance is defined as $\Delta R = \sqrt{(\Delta\eta)^2 + (\Delta\phi)^2}$. Transverse components of particle momenta and energies are given by $p_T = p\sin\theta$ and $E_T = E\sin\theta$.

The pixel detector and inner tracking system consists of three barrel cylinders and three disks in each endcap. The inner-most module is the b-layer of the pixel detector that provides first signal at a radius of 50 mm from the beam line. Vertex finding algorithms require tracks to have hits in this layer in order to discriminate them from photon conversions. The following sub-components are a silicon strip tracker (SCT) in the range $|\eta| < 2.5$ and a transition radiation tracker (TRT) at the outer radii in the range $|\eta| < 2$. TRT signals of leptons and charged hadrons can be discriminated over a wide energy range between $0.5\,\mathrm{GeV}$ and $100\,\mathrm{GeV}$ using X-rays produced by transition radiation. Particles below that energy range do not have enough transverse momentum to pass through the entire tracking system. The pixel detector is surrounded by a superconducting solenoid providing a $2\,\mathrm{T}$ axial magnetic field.

The electromagnetic lead liquid-argon sampling calorimeter (LAr) is divided into three layers called strip, middle and back. Most of the electromagnetic (EM) shower energy is collected in the middle layer with a lateral granularity of 0.025×0.025 in the $\eta \times \phi$ plane. In the strip layer the granularity is finer in η and less fine in ϕ to allow for a precise estimation of the pseudo rapidity and photon direction in order to distinguish from multiple photon showers. The back layer collects energy from very high energy EM showers. The transition region between the barrel and endcap electromagnetic calorimeters covers $1.37 < |\eta| < 1.52$. The endcap EM calorimeters are divided into the inner wheel (EMEC-IW) covering $2.5 < |\eta| < 3.2$ and the outer wheel (EMEC-OW) covering $1.375 < |\eta| < 2.5$. In the region $2.5 < |\eta| < 4.9$ no tracking detector data exists and only energy deposits in the calorimeters are recorded for particles with a minimum transverse energy $E_T > 5\,\mathrm{GeV}$.

The hadronic calorimeter is divided into the barrel and the end-cap partitions. In the barrel, tracks are detected by three longitudinal layers of fine granulated steel and plastic scintillator tiles that are connected to amplifying photomultiplier tubes. The first two layers have a granularity of 0.01×0.01 in the $\eta \times \phi$ plane and the third layer is coarser with 0.02×0.01. The central sector covers $|\eta| < 1$ and two extensions cover $0.8 < |\eta| < 1.7$. The endcap hadronic calorimeters consist of liquid argon absorbers that cover $1.5 < |\eta| < 3.2$ with a granularity of 0.1×0.1 below $|\eta| < 2.5$ and 0.2×0.2 beyond.

The muon spectrometer comprises three large superconducting toroids and a system of trigger and precision tracking chambers. Three cylindrical layers are located in the barrel region at radii between $5\,\mathrm{m}$ and $10\,\mathrm{m}$, which cover the range below $|\eta| < 1$. Three planes perpendicular to the beam in the transition and end-cap region operate in the range $1 < |\eta| < 2.7$. This system is completed by monitored drift

tubes (MDT) in the region $|\eta| < 2$ and cathode strip chambers (CSC) in $2 < |\eta| < 2.7$. The resolution of the muon chamber allows for a precision of about $35\,\mu\mathrm{m}$ in the z-coordinate, $40\,\mu\mathrm{m}$ in the R-coordinate and $5\,\mathrm{mm}$ accuracy related to ϕ.

A transverse plane profile of the ATLAS detector is provided in figure 5.2 in order to illustrate typical penetration depths of particle showers in the dedicated sub-systems. Neutrinos leave no tracks in the detector, while high energetic muons are capable of escaping the detector but leave tracks in the muon spectrometer. Hadronic jets are indicated by the straight path of the neutron and the curved path of the charged proton. Due to its negative charge, the path of the electron is bend into the opposite direction. The photon shower in the electromagnetic calorimeter has a smaller cone radius and is associated with a straight path.

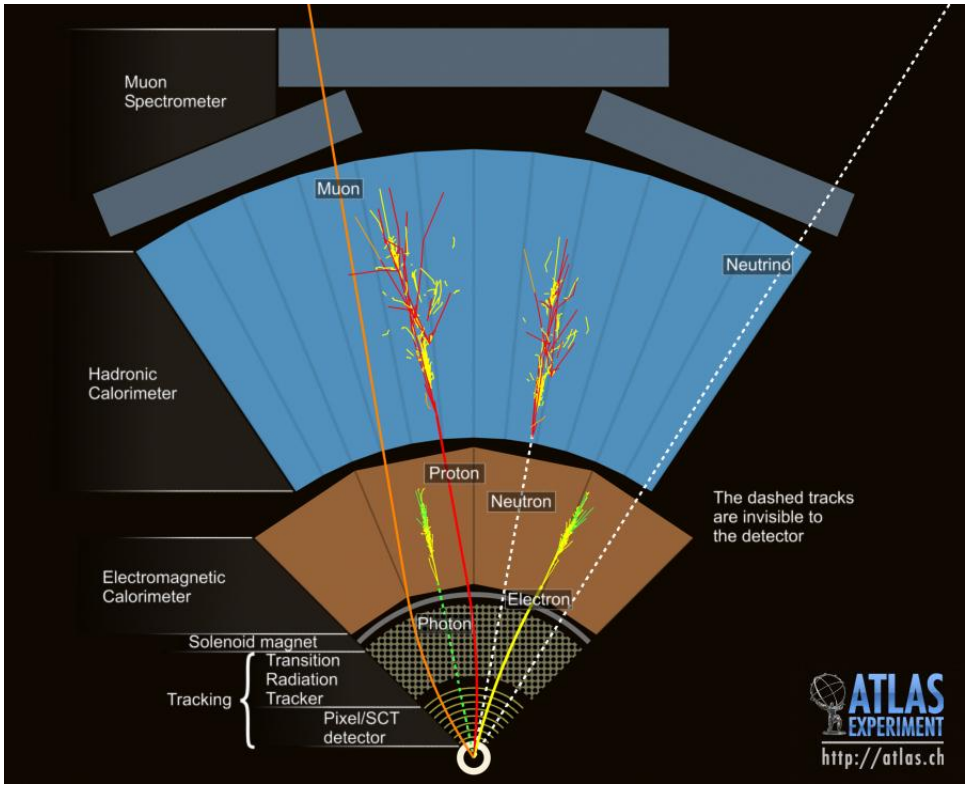

FIGURE 5.2: ATLAS transverse plane profile and subcomponents showing showers of charged and uncharged particles in the hadronic and electromagnetic calorimeters. The muon path indicated that the muon can leave the detector, but provides a signal in the muon spectrometer. The neutrino path is invisible to all sub-detectors.
source: [65]

Figure 5.3 shows the longitudinal profile of the inner detector geometry and illustrates the limits set for the reconstruction of tracks with regard to pseudo rapidity. The two particles that are depicted as red lines have a low transverse momentum of $10\,\mathrm{GeV}$. The track with a pseudo rapidity of $|\eta| = 1.4$ hits detector cells in all three inner layers of the tracking system and provides a rich signal in the transition radiation tracker (TRT). In contrast, the reconstruction of the track with the higher pseudo rapidity of $|\eta| = 2.2$

misses two of the inner layers of the pixel detector and the inner layer of the pixel end-cap. In addition, this track is out of range for the TRT end-cap parts. Tracks above the limit of $|\eta| < 2.5$ do not allow for a sufficient track reconstruction with the pixel detector.

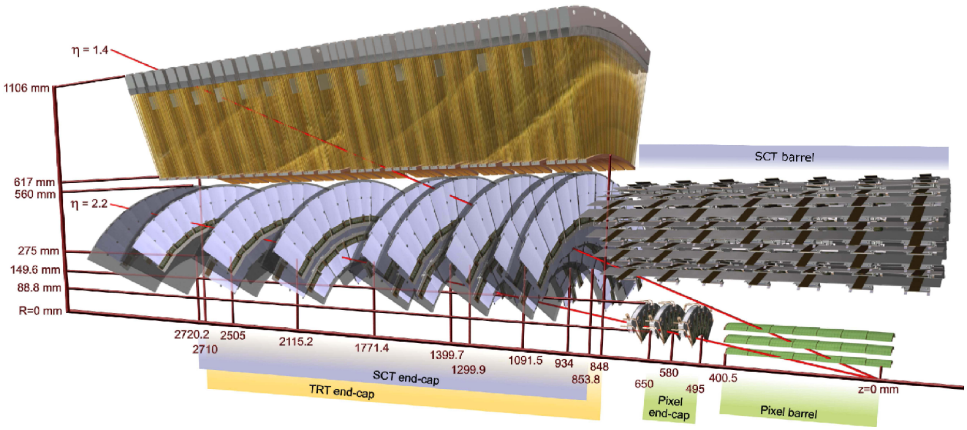

FIGURE 5.3: Inner detector elements hit by two particles with low $pT = 10\,\mathrm{GeV}$. The track with $\eta = 2.2$ crosses only the first layer of the pixel detector and two endcap pixel disks, while the track with $\eta = 1.4$ crosses all three pixel layers. The endcap TRT detection is limited below $|\eta| < 2$ and SCT layers cover up to $|\eta| < 2.5$.
source: [66]

The signal processing is challenged by the short time frame of $50\,\mathrm{ns}$ for the detector readout and the presence of significant pileup. Recorded events have met all requirements of the preceding three level trigger system. The hardware-based first-level trigger (L1) reduces the event rate to a maximum of $75\,\mathrm{kHz}$. Events entering the software-based second-level trigger (L2) have objects with high p_T and have large missing or total energy in the calorimeters or the muon chambers. The reconstruction at L2 is seeded with the full set of detector data within Regions of Interest (RoI) from the L1 result. Reconstructed events are again used to seed the event filter (EF) with a reduced event rate of about $3\,\mathrm{kHz}$. The EF and the L2 trigger are referred to as high-level trigger (HLT), they output an event rate of about $200\,\mathrm{Hz}$ that is processed into data storage and distribution systems. With increased luminosity the HLT event selection got more stringent with event selections based on higher E_T thresholds [67].

5.2 Single top-quark event reconstruction

After offline reconstruction, the event selection follows the final state of next-to-leading order electron+jets and muon+jets signatures of single top-quark and single top-antiquark t-channel events as shown in figure 5.4. The detector signature of the W-decay is searched in form of the electron or muon signal and the neutrino is measured as missing transverse energy. Two hadronic jets are required that can be interpreted as the light quark jet coming from the initial collision and the b-quark jet produced at the Wtb-vertex. The respective rejection of events without b-jets supports the reduction of background signals of W+jet and QCD multijet events that exhibit

similar signatures. A third important source of background signal that is suppressed are $t\bar{t}$ pair-production events that accordingly feature more than one b-jet.

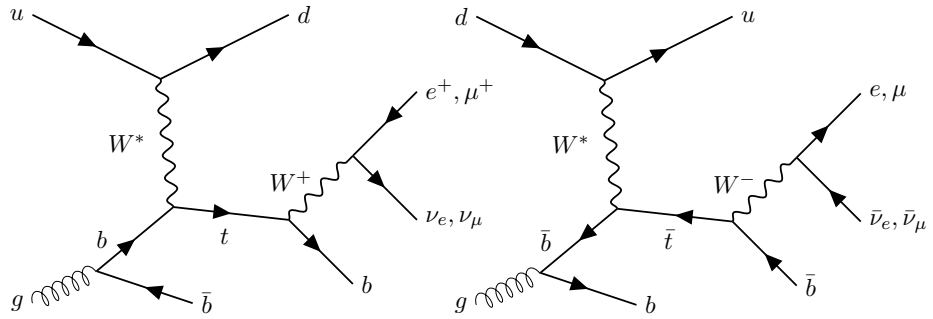

(a) t-channel production and decay for single top-quark

(b) t-channel production and decay for single antitop-quark

FIGURE 5.4: Next-to-leading order Feynman Diagrams for t-channel top-quark (a) and antitop-quark (b) production in the lepton+jets channel. The b-tagged jet and a $W^{\pm}$-boson originate from the decay of the top-quark or top-antiquark. The leptonic particles come from the succeeding decay of the W-boson. The light jet is associated with the initial collision.

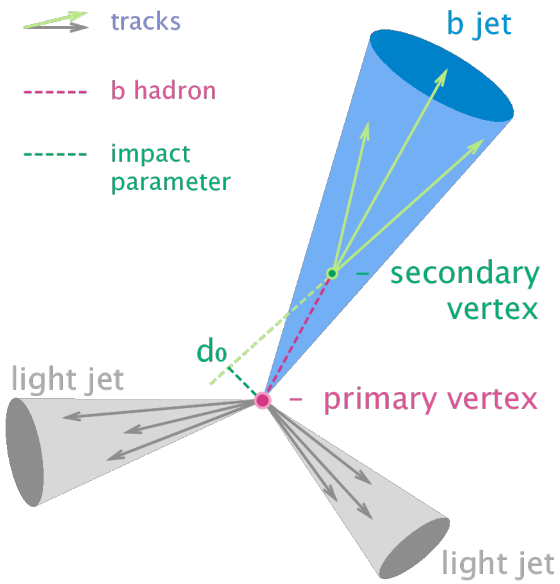

FIGURE 5.5: The b-hadron from the Wtb-vertex decays before it can interact with the pixel detector. It is reconstructed by matching tracks within the b-jet to the displaced secondary vertex. The impact parameters measures the distance between the two vertices in the transverse plane.
source: [68]

The required b-tagging algorithms are also significant for the field of B-physics and for Higgs event reconstruction that has $H \rightarrow b\bar{b}$ as dominant decay channel. Jet flavour tagging needs precise understanding of path reconstruction with the inner detector and involves CPU-intensive training of neural networks. The relatively long lifetime of the b-quark $\tau \approx 1.5 \cdot 10^{-12}\,\mathrm{s}$

leads to a displaced decay at the secondary vertex and causes a large impact parameter d_0, as sketched in figure 5.5. A b-hadron with transverse momentum $p_T = 50\,\mathrm{GeV}$ has a mean transverse flight path projection of $\langle d_0 \rangle = \beta\gamma c\tau \approx 3\,\mathrm{mm}$. The efficiency in avoiding the b-tagging of light quark jets and the success rate in identifying b-jets, which reaches roughly $70\,\%$, are main sources of systematic uncertainties. In order to estimate associated certainty ranges, data-to-simulation scale factors for the tagging efficiencies of bottom-, charm- and light-flavour jets are applied to propagate uncertainties to the final result. A recent comparison of different state of the art algorithms examined by the ATLAS collaboration has been published in [69].

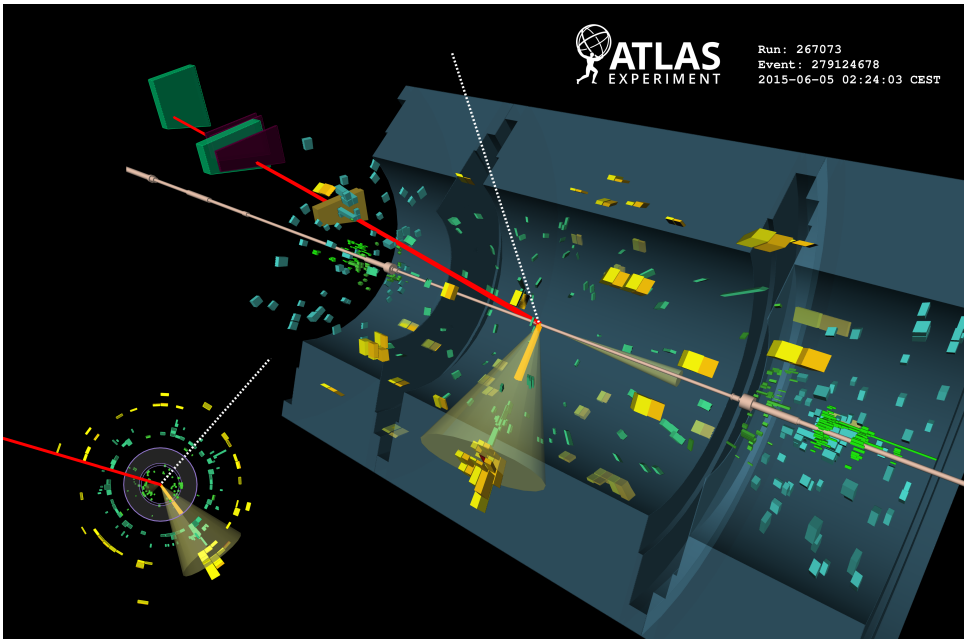

FIGURE 5.6: Event display for t-channel single top-quark production candidate in the muon plus jets channel. The red line represents the reconstructed muon with $p_T \approx 30\,\mathrm{GeV}$. The green and yellow bars show recorded energy deposits in the liquid argon and scintillating-tile calorimeters. The b-tagged jet with $p_{Tb} \approx 50\,\mathrm{GeV}$ is indicated by the larger of the two yellow cones. The cone closer to the beam line represents the untagged jet with $p_{Tl} \approx 40\,\mathrm{GeV}$. The neutrino, displayed as a dotted white line, is associated with $E_T^{\mathrm{miss}} \approx 40\,\mathrm{GeV}$.
source: [70]

Figure 5.6 shows an event display for a single top-quark t-channel candidate. The larger part of the image illustrates a longitudinal profile of the ATLAS detector that is completed by the transverse profile in the lower left corner. Coloured detector tiles highlight the detector signal, while lines and cones depict the reconstructed particles. The b-jet is the central jet with a wider cone radius. The light quark is associated with the forward jet that is observed closer to the beam line.

Reconstruction and event selection are examined using `AnalysisTop (1.11.0)`[1]. Events have passed a good-runs list (GRL) indicating LHC

[1] available at CERN: /cvmfs/atlas.cern.ch/repo/sw/ASG/AnalysisTop/1.11.0

stable beams flag and data quality flags for all detector components and triggers. They have low noise signal in the electromagnetic calorimeter and have at least one reconstructed primary vertex. Object definitions for the reconstruction and conditions for the event selection are applied as follows.

Light jets are reconstructed using the sequential k_t jet recombination algorithm, which is fast, infra-red safe and extends to the collinear region. All selected jets satisfy $p_T > 30\,\mathrm{GeV}$ and $|\eta| < 4.5$. In the transition region $2.7 < |\eta| < 3.5$ between the central and forward hadronic calorimeters, this threshold is raised to $p_T > 35\,\mathrm{GeV}$. An overlap removal is performed for jets that fall in between a distance of $\Delta R < 0.2$ with an electron, as they are likely to correspond to the same physical object. The primary vertex is the one with the largest $\sum p_T^2$ of associated tracks and is taken to be the origin of the hard-scattering collision. If less than 50% of the reconstructed tracks match the primary vertex, it is rejected in order to suppress pileup. This criterion is only applied to jets with $p_T < 50\,\mathrm{GeV}$ and $|\eta| < 2.4$.

Tagged jets are identified using the neural network based algorithm MV1c. The required MV1c result larger than 0.9195 corresponds to an estimated b-tagging efficiency larger than $50\,\%$. The selected b-tagged jet is required to have $pT > 30\,\mathrm{GeV}$. This helps to reduce the contribution of b-jets produced through gluon splitting $g \to b\bar{b}$ that preferably cluster close to the beam axis and have low pT. It also excludes jets for which the b-tagging efficiency is insufficiently low.

Electrons match a reconstructed track through electromagnetic clusters of energy deposits in the electromagnetic calorimeter. They are dressed with photons, which are matched to isolated clusters. Detection of high p_T electrons can result from photon conversions, misinterpreted hadronic jets or from the decay of heavy quarks. Electrons within cone radii of $0.2 < \Delta R < 0.4$ with hadronic jets are rejected. The electron object at trigger level matches either $E_T > 60\,\mathrm{GeV}$ or $E_T > 24\,\mathrm{GeV}$ and an additional isolation criteria. The offline selected electron matches the trigger object and satisfies $p_T > 25\,\mathrm{GeV}$ and $|\eta| < 2.47$. An additional restriction rejects signals from the endcap overlap region $1.37 < |\eta| < 1.52$.

Muons match track segments or complete tracks in the muon spectrometer that can be connected to inner detector tracks. The muon object at trigger level matches either $E_T > 36\,\mathrm{GeV}$ or $E_T > 24\,\mathrm{GeV}$ and an additional isolation criteria. The selected candidates are required to have a transverse momentum $p_T > 25\,\mathrm{GeV}$ and to be in the pseudo rapidity region of $|\eta| < 2.5$. An additional overlap removal is performed to sort out muons from heavy flavor decays. Muons that lie within a cone of $\Delta R < 0.4$ with a hadronic jet of at least $p_T > 25\,\mathrm{GeV}$ are rejected. Additionally, the so-called mini-isolation requirement is applied for a $p_T(\mu)$-dependent cone radius [71].

Neutrinos cannot be detected directly and are identified as missing transverse momentum E_T^{miss}. To conclude the presence of a neutrino, the

difference between the collision energy and the sum of detected energies is calculated from the calibrated three-dimensional calorimeter energy clusters. These are associated with the jets and the lepton tracks including calorimeter clusters that were not matched to any track. In the event selection this reconstruction must satisfy $E_T^{\text{miss}} > 30\,\text{GeV}$.

An additional veto is applied in requiring that the invariant mass of the combined lepton and b-jet system agrees with $m(l,b) < 160\,\text{GeV}$. This excludes the higher energy region, because the underlying matrix-element calculation of Monte Carlo generators does not reliably model off-shell effects.

Targeting misinterpreted electrons from multijet events, the multijet veto defines two additional cuts. The W-boson mass has to satisfy $m_T(W) > 50\,\text{GeV}$ according to equation 5.5. Equation 5.6 defines an additional isolation threshold relative to the jet j_1 with the highest p_T, which primarily targets leptons with low p_T.

$$m_T(W) = \sqrt{2p_T(l)E_T^{\text{miss}}\left(1-\cos\Delta\phi(l,E_T^{\text{miss}})\right)} > 50\,\text{GeV} \tag{5.5}$$

$$p_T(l) > 40\,\text{GeV}\left(1-\frac{\pi-|\Delta\phi(j_1,l)|}{\pi-1}\right) \tag{5.6}$$

The above list of criteria accepts events containing secondary leptons that have lower p_T than the primary lepton. Events with secondary leptons of same flavour like the primary lepton are rejected, if the combined invariant mass matches $80\,\text{GeV} < m(l_1,l_2) < 100\,\text{GeV}$. All events with secondary leptons in a cone closer than $\Delta R < 0.4$ to the b-jet are rejected as well. Additionally, secondary leptons satisfy $p_T(l) > 10\,\text{GeV}$ and $|\eta| < 2.5$ for muons compared to $|\eta| < 4.9$ for electrons. The dilepton veto significantly reduces backgrounds from Z+jets ($-49.1\,\%$ for electrons and $-32.6\,\%$ for muons) and $(t\bar{t}, tW, t\bar{b})$-production ($-21.1\,\%$ for electrons and $-20.8\,\%$ for muons).

5.3 Results from ATLAS $8\,\text{TeV}$ run

Given a selected event, the top-quark mass can be reconstructed from the sum of the four-vectors of the W-boson and the b-jet. The W-boson mass can be calculated from the lepton system within some uncertainty coming from the unresolved z-component of the neutrino.

After modelling of background expectations, which are verified within control regions, several kinematic variables are combined to one discriminant in order to apply a neural network (NN) to separate signal from background events. This comprises invariant masses, transverse masses, pseudorapidities, angles measured in the top-quark rest-frame and transverse momenta of different particle combinations. The most correlated variables are removed in a preprocessing algorithm and the seven that are most discriminating are used for the training of the network. This set involves the invariant masses of the top-quark $m(l\nu b)$, the jets $m(jb)$, the combined lepton and b-jet system $m(lb)$ and the transverse mass of the reconstructed W-boson $m_T(l, E_T^{\text{miss}})$. Two more are added with the pseudorapidity of the untagged jet $|\eta(j)|$ and the difference in pseudorapidities of the W-boson

and the b-tagged jet $\Delta\eta(l\nu b)$. The last variable used is the cosine $\cos\theta^*(l,j)$ of the angle between the charged lepton and the untagged jet.

A maximum likelihood fit to the entire output distribution of the neural network is performed, which yields the expectation values of the numbers of t-channel single top-quark and single top-antiquark events according to equation 5.1, which are given in equations 5.7 and 5.8.

$$\hat{\nu}(tq) = 11848 \pm 195 \tag{5.7}$$

$$\hat{\nu}(\bar{t}q) = 6921 \pm 174 \tag{5.8}$$

Main sources of uncertainties are related to the energy scale and resolution corrections for the reconstruction of the lepton and jets, as well as to the b-tagging efficiency. Additionally, important uncertainties are associated with the background estimation. Systematic effects are estimated by comparing different MC generators, PDF sets and scale variations. The luminosity uncertainty for the analysed 2012 data is $1.9\,\%$ [72]. The quoted uncertainties on $\hat{\nu}$ are obtained statistically from pseudo experiments and propagated to the fiducial cross-section.

The fiducial cross-section is calculated following equation 5.4 with a simulated ratio $N_{\text{fid}}/N_{\text{sel}} \approx 5$ and the inclusive cross-section is extrapolated according to equation 5.2 using a simulated fiducial acceptance $A_{\text{fid}} \approx 17\,\%$. The results and the estimated uncertainties are quoted in table 5.1. They are in good agreement with the SM predictions for the inclusive cross-sections, which were discussed in detail in chapter 3 and are repeated in the last column of table 5.1 for comparison.

The underlying cause for the mass dependence of the fiducial cross-section is the simulated value of $N_{\text{fid}}/N_{\text{sel}}$ and the neural network fit. Using different MC generators, the measurement was repeated with $m_t^{\text{MC}} = 172.5 \pm (2.5, 5, 7.5)\,\text{GeV}$ followed by a linear fit of $\sigma_{\text{fid}}(m_t^{\text{MC}})$ according to equation 4.1. The obtained absolute and relative mass dependencies are quoted in table 5.1. They contribute to the mass dependence of the inclusive cross-section, which is additionally affected by the mass dependence of the fiducial acceptance. This is analysed in detail in chapter 6.

The combined result is visualised in figure 5.7, applying the technique introduced for the indirect mass measurement in chapter 4. Figure 5.7a, neglecting the experimental uncertainty, demonstrates almost parallel curves of the obtained result and the theoretical expectations. Figure 5.7b shows sampled pseudo experiments for both distributions with a width of plus-minus two standard deviations. The marginal likelihood function extracted from the multiplication of these samples has a large central interval, extending from $m_t^{0.16} = 149.3\,\text{GeV}$ to $m_t^{0.84} = 190.0\,\text{GeV}$. Furthermore, it does not exhibit a clear maximum in this interval. Thus, the defined method for the indirect mass measurement is not applicable in this scenario.

	$\sigma^{\text{exp}}[\text{pb}]$	$\Delta^{-}_{\text{unc.}}[\text{pb}]$	$\Delta^{+}_{\text{unc.}}[\text{pb}]$	$\delta\left[\frac{\text{pb}}{\text{GeV}}\right]$	$\bar{\delta}\left[\frac{\%}{\text{GeV}}\right]$	$\sigma^{\text{theo.}}[\text{pb}]$
$\sigma_{\text{fid}}(tq)$	9.78	-0.57(5.8 %)	0.57(5.8 %)	-0.06	-0.60	
$\sigma_{\text{fid}}(\bar{t}q)$	5.77	-0.45(7.8 %)	0.45(7.8 %)	-0.04	-0.69	
$\sigma_{\text{inc}}(tq)$	56.7	-3.8(6.7 %)	4.3(7.6 %)	-0.59	-1.04	55.6 ± 2.3
$\sigma_{\text{inc}}(\bar{t}q)$	32.9	-2.7(8.2 %)	3.0(9.1 %)	-0.37	-1.12	30.3 ± 1.5
$\sigma_{\text{inc}}(tq + \bar{t}q)$	89.6	-6.3(7.0 %)	7.1(7.9 %)	-0.96	-1.07	85.9 ± 3.8

TABLE 5.1: ATLAS measurement for fiducial and inclusive single top-quark t-channel cross-sections and their mass dependence. The result is fitted to a linear function according to equation 4.1 and the absolute and relative mass dependence are derived from the fit according to equations 3.14 and 3.15. The fits are fixed to the cross-section for the reference top-quark mass at 172.5 GeV. For comparison, theory predictions are given in the last column, all other quantities are quoted from [58].

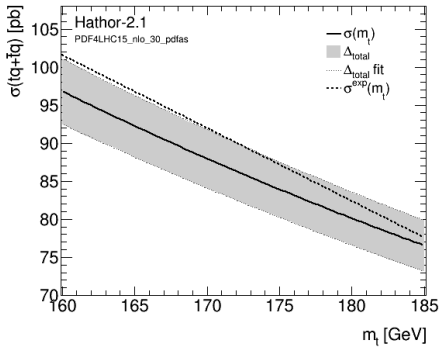

(a) Linear fits for the experimental result according to equation 4.1 compared to the theory prediction that is fitted to equation 3.13.

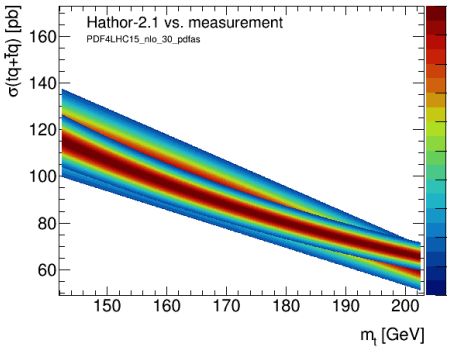

(b) Measurement and expectation sampled by pseudo experiments as discussed for figure 4.3. The distribution in the background samples the experimental result using $\Delta^{\text{exp}} = 7.1\,\text{pb}$. The curve in the foreground samples the theory calculations.

FIGURE 5.7: The experimental result fitted to $\sigma^{\text{exp}} = 89.6\,\text{pb} - 0.96\,\frac{\text{pb}}{\text{GeV}}(m - 172.5\,\text{GeV})$. The difference to the theoretical mass dependence of $-0.81\,\frac{\text{pb}}{\text{GeV}}$ is too low to apply the indirect top-quark mass measurement. Uncertainties in (a) indicate plus-minus one standard deviation and uncertainties in (b) depict a width of plus-minus two standard deviations.

6. Simulation of the fiducial acceptance

Contributions to the observed mass dependence of the fiducial cross-section measurement emerge from the simulation of the event selection. On the right side of equation 5.4, the luminosity $\mathcal{L}_{\text{int}}$ is independent of the assumed top-quark mass, but the expectation value for the number of observed events $\hat{\nu}$ and the simulation of $N_{\text{fid}}/N_{\text{sel}}$ are mass dependent. This combines with the dependence on A_{fid} in the extrapolation to the inclusive cross-section, which is used for the indirect mass measurement. In this chapter the dependence of the fiducial acceptance on m_t^{MC} is subdivided into contributions from individual partial selection cuts.

6.1 Event simulation

The presented analysis is based on virtual pp-collision events generated with `PowHegBox` [73] and `Pythia8` [74]. Uncertainties related to the choice of the MC generator are usually addressed by comparing the results using different MC generators. However, this part of the analysis is beyond scope for this thesis. The same event sets can be deployed to examine detector simulations in order to analyse the total event selection efficiency. Simulation also plays a crucial role in the signal background separation, because the virtually detected particles carry the information about their production process. This level of extended information is referred to as MC Truth.

The probabilistic nature of quantum processes is implemented with the help of pseudo random number generators. It is in general not determined at what time and via which channel a particle will decay, hence related probability distributions emerge in all involved virtual interaction vertices.

Virtual hadronic collisions are produced aiming to observe hard scatterings of the randomly distributed partons within the hadrons. The probability distribution is modelled by the underlying PDF. When short lived particles like the top-quark are produced in the process of the deep inelastic scattering, the spin information is transmitted from the partons to the decay products. A central task is to model the hadronisation of color charged particles using Pythia8. Many of the recombinations are again unstable and decay within a short range of time and space. Thus, the decay chain is modelled through a sequence of stages as a cascade of successive branchings. Besides the main collision and its decay products, additional parton showers originating from initial and final state radiation are modelled to support the important distinction between those phenomena. The collision rates and multiplicities observed in the ATLAS detector are simulated in both, pileup conditions meaning multiple hadrons collide at the same time, and multiple parton interactions meaning more than one hard scattering within the same hadronic collision.

The PowHegBox combines matrix element methods (ME) for the hard process and parton shower techniques (PS) for the soft and collinear emissions in the so-called NLO-matching method [75]. Matrix element methods implement the series expansion in powers of α_s. Diverging elements in the underlying mathematical treatment limit the overall applicability for collinear particles and for collisions where one parton energy vanishes, hence cut off values have to be adapted for this simulation. In this regime and with the rising number of involved particles, iterative parton shower (PS) methods are used that are more probabilistic and more approximative. The PS result is subtracted from the diverging ME result, but since it is not guaranteed that the result is always positive, a small fraction of events gets negative event weights to correct this issue [76, 73]. Thus, for very small count rates there is certain probability to simulate negative cross-sections. However, this can be neglected for the number of events used in this analysis.

6.2 Event selection

This analysis uses events modelling the t-channel lepton+jets process. Sets contain either top-quarks or top-antiquarks only. All contained events feature exactly one charged lepton and the neutrino, which originate from the leptonic decay of the W-boson. Contrary to reconstruction methods, which may confuse these particles with products of hadronic or τ decay, the truth level information allows for this attribution.

For the event selection, the class TopFiducial, which is contained in AnalysisTop(1.11.0), has been adapted in order to select particles accepted for the fiducial volume. The order of the cuts has been arranged in order to distinguish between cuts on the lepton attributes, cuts on jet related parameters and cuts that effect both. Additionally, new features have been included in order to enable the user to configure the minimum pT that is used to cut off soft hadronic and leptonic jets.

In the first cut, all events that do not contain a selectable electron or muon are rejected. The remaining events are referred to as being in the electron or muon channel. The selected lepton is dressed with photons within a $\Delta R < 0.1$, the final four-vector is the sum of the four-vectors of the dressing photons and the original lepton. The selected lepton satisfies $pT_l > 25\,\mathrm{GeV}$ and $|\eta| < 2.5$.

In the four subsequent cuts, events with less or more than exactly one untagged jet and exactly one b-tagged jet are rejected. Both hadronic jets satisfy $pT > 30\,\mathrm{GeV}$. The untagged jet is allowed in the region $|\eta| < 4.5$, whereas the central b-tagged jet must satisfy $|\eta| < 2.5$.

Two additional cuts are added, which use combined jet and lepton properties. They have been shifted to the end of the cut sequence, in order to separate clearly between jet- or lepton-related cuts and cuts involving both. The first cuts on the invariant mass of the combined lepton and b-jet system, which is required to match with the condition $m(lb) < 160\,\mathrm{GeV}$ in order to exclude the off-shell region. In general, off-shell effects are not included in the matrix-element calculation. The last cut performs the overlap removal, which asserts that the selected lepton and the jets have a minimum distance of $\Delta R \geq 0.4$. For $\Delta R < 0.2$ the closest jets overlapping with

electron candidates are subsequently rejected, for $\Delta R < 0.4$ electron candidates are subsequently rejected. However, this cut has a low contribution independent of its position in the cut-sequence.

6.3 Mass dependence of the event selection

The notation for the mass dependent acceptances is defined in equation 6.1, where the index i refers to the cut number and $l \in (e, \mu, e+\mu)$ and $q \in (t, \bar{t}, t+\bar{t})$. The sum of weights for the complete data set before any cut is denoted as $N(m, q)$ and the sum of weights of selected events is given as $\nu(m; l, q)$. The MC mass was set to seven values $m_t^{\mathrm{MC}} = 172.5 \pm \Delta m\,\mathrm{GeV}$ using $\Delta m \in (0, 2.5, 5, 7.5)\,\mathrm{GeV}$.

$$\epsilon_i(m_t; l, q) = 100 \cdot \frac{\nu(m; l, q)}{N(m; q)} \tag{6.1}$$

The analysis can be carried out either separated into electron and muon channels or with combined lepton+jets acceptances. In the following, combined $\epsilon_i(m; e+\mu, t)$ data will serve for illustration. The respective acceptances can be combined by simple addition as described by equation 6.2, since the lepton channels are disjunct and e- and μ-channel data comes from the same weighted data set. For top-quark and top-antiquark acceptances, which come from different weighted sets, the combination by weighted mean yields equation 6.3.

$$\epsilon_i(m; e+\mu, q) = \frac{\nu(m; e, q) + \nu(m; \mu, q)}{N(m; q)} \tag{6.2}$$

$$\epsilon_i(m; l, t+\bar{t}) = \frac{\nu(m; l, t) + \nu(m; l, \bar{t})}{N(m; \bar{t}) + N(m; t)} \tag{6.3}$$

The acceptance after execution of all cuts can be used for the solution of equation 5.2. The results for all sets are listed in table 6.1.

Figure 6.1a demonstrates that a linear fit according to equation 6.4 describes the data very well. For the top-quark sets the fit result for the fiducial acceptance is $\epsilon(t) = 17.22\,\% + 0.074\,\frac{\%}{\mathrm{GeV}}$ and for the top-antiquark it is $\epsilon(\bar{t}) = 17.46\,\%{+}0.076\,\frac{\%}{\mathrm{GeV}}$. The fit quality is very good with $x^2/\mathrm{NDF} = \mathcal{O}(0.1)$. The fiducial acceptance for the reference mass at $\Delta m = 0$ can be extracted from the fit and can be identified with $\bar{\epsilon}$. In order to compare the mass dependence for different cuts, it has to be normalised to the relative mass dependence $\bar{\delta}$ following equation 6.5. This centres the linear function in the origin and yields the relative mass dependence on the result as the slope, which is found to be $\bar{\delta}(t) = 0.43\,\frac{\%}{\mathrm{GeV}}$ and $\bar{\delta}(\bar{t}) = 0.44\,\frac{\%}{\mathrm{GeV}}$.

$$\epsilon(\Delta m) = \bar{\epsilon} + \delta \cdot \Delta m \tag{6.4}$$

$$\frac{\epsilon(\Delta m) - \bar{\epsilon}}{\bar{\epsilon}} = \frac{\delta}{\bar{\epsilon}} \Delta m = \bar{\delta} \Delta m \tag{6.5}$$

Throughout the sequence of cuts, the comparison of acceptances between top-quarks and top-antiquarks, as well as between the electron and the muon channel show less or more difference. However, the aim of this

process	m_t^{MC}[GeV]	ID	size $[10^6]$	$A_{\mathrm{fid}}[\%]$
$tq(l+\mathrm{jets})$	165.0	110268	3	16.65
$tq(l+\mathrm{jets})$	167.5	110270	3	16.80
$tq(l+\mathrm{jets})$	170.0	110272	3	17.04
$tq(l+\mathrm{jets})$	172.5	110070	5	17.26
$tq(l+\mathrm{jets})$	175.0	110274	3	17.43
$tq(l+\mathrm{jets})$	177.5	110276	3	17.59
$tq(l+\mathrm{jets})$	180.0	110278	3	17.73
$\bar{t}q(l+\mathrm{jets})$	165.0	110269	2	16.86
$\bar{t}q(l+\mathrm{jets})$	167.5	110271	2	17.07
$\bar{t}q(l+\mathrm{jets})$	170.0	110273	2	17.31
$\bar{t}q(l+\mathrm{jets})$	172.5	110071	5	17.52
$\bar{t}q(l+\mathrm{jets})$	175.0	110275	2	17.59
$\bar{t}q(l+\mathrm{jets})$	177.5	110277	2	17.85
$\bar{t}q(l+\mathrm{jets})$	180.0	110279	2	18.02

TABLE 6.1: Set ID and number of events rounded to 10^6 for analysed PoweHeg+Pythia8 datasets. The simulated fiducial acceptances are extracted as the centre point from the linear fit result.

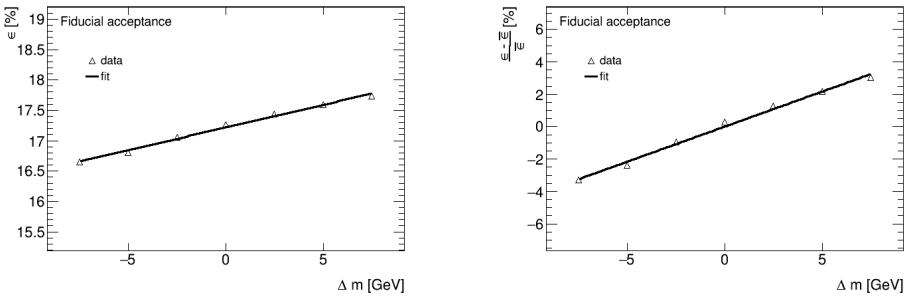

(a) Fiducial acceptance as linear function of the MC top mass according to equation 6.4. The centre point is extracted as $A_{\mathrm{fid}} = \bar{\epsilon}$ and the slope is the absoulte mass dependence δ.

(b) Normalised fiducial acceptance according to equation 6.5. The function is centred to the origin and the slope is the relative mass dependence $\bar{\delta}$.

FIGURE 6.1: Fiducial acceptance with absolute mass dependence δ (a) and normalised to extract the relative mass dependence $\bar{\delta}$ (b). The same strategy is applied to analyse the acceptances and mass dependencies of intermediate cuts.

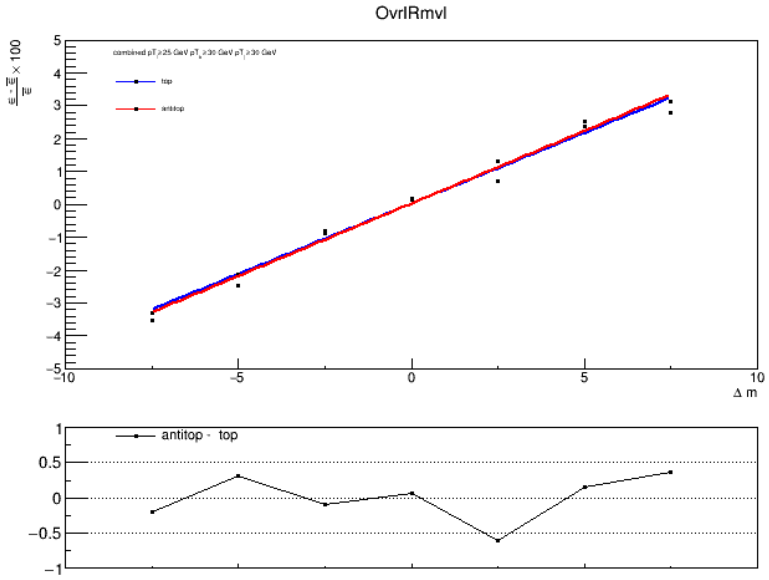

FIGURE 6.2: A comparison of the relative mass dependencies of top-quarks and top-antiquark shows no relevant differences within the statistical variance. The lower axes show the difference between the normalised data points.

analysis is to examine the relative mass dependencies, which agree well for the top-quark and the top-antiquark sets throughout the cut sequence. This is illustrated by the graph shown in figure 6.2 where the lower axes show the difference between the data points after normalisation. Within the variance of the data around the linear fit, equal relative mass dependencies can be concluded. The same is valid for the comparison between the electron and the muon channel. While unnormalised fits may exhibit slightly different results, the relative acceptances are in very good agreement. The same analysis carried out on weighted and unweighted data sets can exclude a mass dependence introduced by the MC event weighting.

An overview providing the fit results for the complete cut sequence is given in table 6.2 for the top-quark sets and in table 6.2 for the top-antiquark sets. The mass dependence of the fiducial acceptance primarily comes from the first two cuts sorting out events, which do not contain a selectable lepton or have less than two reconstructed jets. These are the cuts with the highest cut efficiencies. In contrast, subsequent cuts on the jet multiplicity reduce the mass dependence, which leads to a maximum after the second cut. In fact, the jet selection is a commutative subsequence, which results in accepting events with exactly one untagged jet and exactly one b-tagged jet after the fifth cut. The last two cuts have comparably small cut efficiencies and do not significantly change the mass dependence.

i	selection	$\bar{\epsilon}_i$ [%]	$\delta_i \left[\frac{\%}{\text{GeV}}\right]$	$\delta_i/\bar{\epsilon}_i \left[\frac{\%}{\text{GeV}}\right]$
1	minimum 1 e|mu	46.33	0.104	0.22
2	minimum 2 jets	32.49	0.166	0.51
3	minimum 1 light jet	30.56	0.153	0.50
4	exactly 1 untagged jet	22.41	0.103	0.46
5	exactly 1 b-taggged jet	17.86	0.076	0.42
6	$m(lb) < 160\,\text{GeV}$	17.41	0.073	0.42
7	overlap removal	17.22	0.074	0.43

TABLE 6.2: Acceptances and mass dependencies for all selection cuts in the simulation of the fiducial acceptance for single top-quarks.

i	selection	$\bar{\epsilon}_i$ [%]	$\delta_i \left[\frac{\%}{\text{GeV}}\right]$	$\delta_i/\bar{\epsilon}_i \left[\frac{\%}{\text{GeV}}\right]$
1	minimum 1 e|mu	47.88	0.095	0.20
2	minimum 2 jets	32.46	0.164	0.51
3	minimum 1 light jet	30.36	0.153	0.51
4	exactly 1 untagged jet	22.62	0.102	0.45
5	exactly 1 b-taggged jet	18.10	0.076	0.42
6	$m(lb) < 160\,\text{GeV}$	17.65	0.074	0.42
7	overlap removal	17.46	0.076	0.44

TABLE 6.3: Acceptances and mass dependencies for all selection cuts in the simulation of the fiducial acceptance for single top-antiquarks.

6.4 Extrapolation to the inclusive cross section

To propagate above results, the normalised fit of the fiducial acceptance, according to equation 6.5, can be plugged into equation 5.3 defining the inclusive cross-section. This is presented in equation 6.6, where the central results are denoted as $\bar{A}_{\text{fid}}$ and $\bar{\sigma}_{\text{inc}}$.

$$\sigma_{\text{inc}}(m - m_{\text{ref}}) = \frac{1}{(1+\bar{\delta}m)} \underbrace{\frac{1}{\bar{A}_{\text{fid}}} \frac{N_{\text{fid}}}{N_{\text{sel}}} \frac{\hat{\nu}}{\mathcal{L}_{\text{int}}}}_{:=\bar{\sigma}_{\text{inc}}} \tag{6.6}$$

$$\approx \bar{\sigma}_{\text{inc}} \left(1 - \bar{\delta}m\right) \tag{6.7}$$

The last approximation stated with equation 6.7 can be derived by application of a Taylor series at the central point m_{ref} to the exact expression $\sigma_{\text{inc}}(m - m_{\text{ref}}) = \bar{\sigma}_{\text{inc}} \left(1 + \bar{\delta}m\right)^{-1}$. The derivatives can be written in compact form as in equation 6.8 and the evaluation for $m = 0$ simplifies this expression to equation 6.9. Plugging this into a Taylor series as written in 6.10 yields the series formula 6.11 that models propagation of the mass dependence from the fiducial acceptance to the inclusive cross-section.

$$\sigma^{(n)}(m - m_{\text{ref}}) = \bar{\sigma} \cdot (-1)^n \cdot n! \left(1 + \bar{\delta}m\right)^{-(n+1)} \cdot \left(\bar{\delta}\right)^n \tag{6.8}$$

$$\sigma^{(n)}(m_{\text{ref}}) = \bar{\sigma} \cdot n! \cdot \left(-\bar{\delta}\right)^n \tag{6.9}$$

$$\tilde{\sigma}_N(m - m_{\text{ref}}) = \sum_{n=0}^{N} \frac{1}{n!} \sigma^{(n)}(0) \cdot m^n \tag{6.10}$$

$$= \bar{\sigma} \cdot \sum_{n=0}^{N} \left(-\bar{\delta}m\right)^n = \bar{\sigma} \left(1 - \bar{\delta}m + \left(\bar{\delta}m\right)^2 - \left(\bar{\delta}m\right)^3 \cdots\right) \tag{6.11}$$

This series comprises a very sufficient first order approximation. The linearisation error can be bounded by the estimation given in equation 6.12. With the obtained result $\bar{\delta} = 0.43\%$ it scales to 0.01% in an interval $|m| \leq 1\,\text{GeV}$. In the examined range $|m| \leq 7.5\,\text{GeV}$ the error can be estimated to roughly 0.1%.

$$\frac{|\tilde{\sigma}_1(m - m_{\text{ref}}) - \sigma(m - m_{\text{ref}})|}{\bar{\sigma}} \leq \left(\bar{\delta}m\right)^2 \tag{6.12}$$

This simple analysis shows that the mass dependence of the fiducial acceptance can be translated directly to the respective mass dependence propagated to the extrapolated inclusive cross-section by just changing the sign. This agrees well to the fits carried out on the ATLAS results for the fiducial and inclusive cross-sections that is presented in table 5.1. The fits yield $\sigma_{\text{inc}}(tq) = 56.7\,\text{pb} - 0.59\,\frac{\text{pb}}{\text{GeV}} \cdot m$ for the top-quark and $\sigma_{\text{inc}}(\bar{t}q) = 32.9\,\text{pb} - 0.37\,\frac{\text{pb}}{\text{GeV}} \cdot m$ for the top-antiquark. This corresponds to the relative mass dependencies $\bar{\delta}_{\text{inc}}(tq) \approx 1.04\%$ and $\bar{\delta}_{\text{inc}}(\bar{t}q) \approx 1.12\%$. The subtraction of the contributions of the fiducial extrapolation that were found in this chapter, precisely $\bar{\delta}(tq) \approx 0.43\%$ and $\bar{\delta}(\bar{t}q) \approx 0.44\%$, yields the expectations $\bar{\delta}_{\text{fid}}(tq) \approx 0.61\%$ and $\bar{\delta}_{\text{fid}}(\bar{t}q) \approx 0.68\%$. When rescaling this to the ATLAS results for the fiducial cross-section the expectations for its absolute mass dependence are $\sigma_{\text{inc}}(tq) = 9.78\,\text{pb} - 0.06\,\frac{\text{pb}}{\text{GeV}} \cdot m$ for the top-quark and $\sigma_{\text{inc}}(\bar{t}q) = 5.77\,\text{pb} - 0.04\,\frac{\text{pb}}{\text{GeV}} \cdot m$ for the top-antiquark. This matches with

the mass dependencies quoted in table 5.1, which were fitted directly using the fiducial cross-section data.

7. Mass dependence on transverse momentum thresholds

The selection cuts associated with the largest contributions to the mass dependence discriminate on either lepton or jet attributes. Limiting selection criteria are based on the pseudorapidity and the transverse momentum. The margin for the pseudorapidity is strictly fixed by the detector geometry. Thus, as an ansatz to reduce the mass dependence, different thresholds for the minimum transverse momentum of the lepton, the b-tagged jet and the untagged jet $\epsilon(m; p_T) = \epsilon(m; (p_T(\ell), p_T(b), p_T(j)))$ are examined in this chapter. The applied `AnalysisTop` version has been extended to the functionality that threshold settings can be passed as function arguments to the jet, electron and muon selection. Starting from the default setting $(p_T(\ell), p_T(b), p_T(j)) = (25, 30, 30)\,\mathrm{GeV}$, 27 selections have been compared, in which the values are changed independently to $p_T(\ell, b, j) \in (20, 25, 30)\,\mathrm{GeV}$. Combined $(e + \mu)$-channel data is used for illustration in the following analysis. Section 7.1 focuses on the contribution from the lepton-related first cut, and additional contributions from the jet-related cuts number two to five are examined in section 7.2.

7.1 Minimum transverse momentum of the lepton

The single-muon trigger [77] and the electron trigger [78] settings comprise the threshold $p_T(\ell) > 24\,\mathrm{GeV}$. This makes the lower value $p_T(\ell) = 20\,\mathrm{GeV}$ somewhat hypothetic, but nevertheless, the analysis can support the understanding of the mass dependence of the lepton selection. It is placed at the beginning of the cut sequence, allowing to distinguish between e^+, e^-, μ^+ and μ^- channels. By rejection of well more than 60% of the events in any observed scenario, it contributes the highest cut efficiency. The commutativity of the cut order with regard to the acceptances and their mass dependencies was found to be observable as expected, but cut efficiencies naturally depend on the cut order. However, they are less meaningful for this analysis.

Figure 7.1 shows the mass dependence for the three applied threshold settings for the complete cut sequence. The parallel curves clearly show that the lepton threshold only affects the lepton selection. The differences between the relative mass dependencies, which are introduced in the first cut, equal the differences after the jet-related cuts in all observed scenarios. Negligible differences of $0.01\,\%$ occur only after the last two cuts including lepton attributes. Table 7.1 shows that using the lower threshold, the relative mass dependence can be slightly reduced, while it increases for the

raised setting. Higher thresholds naturally decrease the associated acceptances.

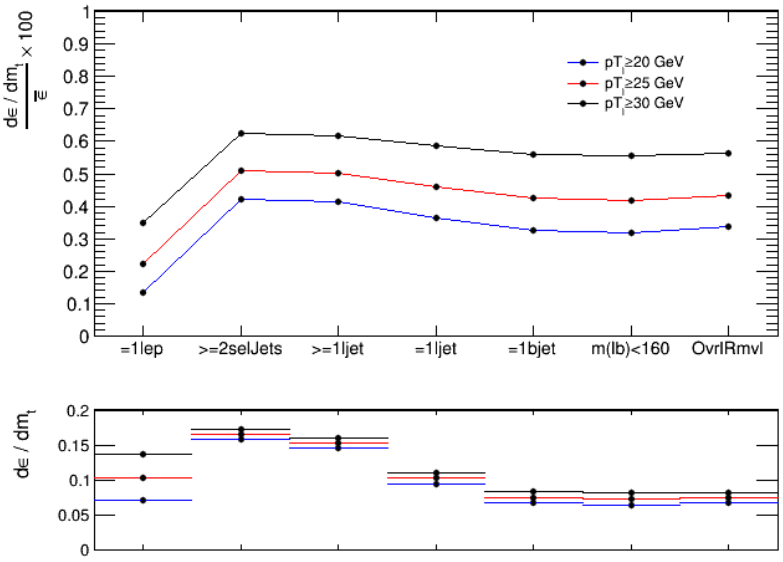

FIGURE 7.1: The upper axes display the relative mass dependencies and the lower axes show the absolute values for the three threshold settings $p_T(\ell) = 20, 25, 30\,\mathrm{GeV}$. The mass relative dependence decreases with the threshold requirement. The plot shows the results for the top-quark sets, which are in good agreement with the results for top-antiquark sets.

particle	$p_T(\ell)$	$\bar{\epsilon}(\ell)$	$\bar{\delta}(\ell)$	$\bar{A}_{\mathrm{fid}}$	$\bar{\delta}$
top	30 GeV	39.32	0.35	14.51	0.57
top	25 GeV	46.33	0.22	17.22	0.43
top	20 GeV	53.40	0.13	19.93	0.34
antitop	30 GeV	40.75	0.33	14.76	0.58
antitop	25 GeV	47.88	0.2	17.46	0.44
antitop	20 GeV	55.04	0.11	20.14	0.34

TABLE 7.1: Acceptances for $p_T(\ell)$ threshold variations after the first cut requiring exactly one lepton. The last two columns show the resulting fiducial acceptances and the associated relative mass dependencies.

7.2 Minimum transverse momentum of the hadronic jets

A higher top-quark mass can be expected to correlate with a higher transverse momentum of the b-tagged jet, because it is produced in the top-quark decay at the Wtb-vertex. The implication for the light-jet and hadronic jets from initial and final state radiation is less conclusive. The acceptance for

jets from ISR and FSR, which cluster in the collinear region and preferably have low p_T, can be expected to increase for lower threshold settings. The limits used in the ATLAS measurement are set to $p_T(j,b) > 30\,\mathrm{GeV}$ with regard to low reconstruction efficiencies in the low p_T regime. However, in contrast to the lepton trigger, the HLT configuration allows data taking using the lower value of $p_T(j,b) = 20\,\mathrm{GeV}$ [79].

The one-dimensional distributions of the multiplicities of light jets and b-jets in the simulated data exhibit distinct maxima for a jet multiplicity of one. Consequently, the two-dimensional distribution has a maximum for the selected bin counting exactly one untagged and exactly one b-tagged jet. This can be observed in table 7.2 for the top-quark sets and in table 7.4 for the top-antiquark sets using the default setting $p_T(j,b) = 30\,\mathrm{GeV}$. Tables 7.3 and 7.5 allow to compare the same distributions for the lowered threshold $p_T(j,b) = 20\,\mathrm{GeV}$.

The distribution is calculated after the cut on the lepton using combined lepton channels. Thus, the sum of weights for each jet multiplicity $\nu(b,j)(m)$ is divided by $\nu(\ell)(m)$ relating to $100\,\%$. The associated division by $\nu(\ell)(m)$ is carried out for each set, which consequently cancels the mass dependence introduced by the first cut, as demonstrated with equations 7.1 and 7.2. This provides a way to measure the mass dependence $\delta(b,j)$ of the single bins in the distribution of the jet multiplicities.

$$\frac{\nu(b,j)}{\nu(\ell)}(m) \approx \frac{\bar{\nu}(b,j)\cdot(1+\bar{\delta}(\ell)\cdot m)\cdot(1+\bar{\delta}(b,j)\cdot m)}{\bar{\nu}(\ell)\cdot(1+\bar{\delta}(\ell)\cdot m)} \tag{7.1}$$

$$\approx \frac{\bar{\nu}(b,j)}{\bar{\nu}(\ell)}\cdot(1+\bar{\delta}(b,j)\cdot m) \tag{7.2}$$

In each bin, the mass dependent data is fitted and normalised to the central result for $m_t = 172.5\,\mathrm{GeV}$, equivalent to equations 6.4 and 6.5. The positive and negative numbers for the particular jet multiplicities in tables 7.2 up to 7.5 represent the obtained relative mass dependencies and the parenthesised numbers represent the central values extracted from the fits.

All events with more than one selectable b-jet are conflated to the last column and all events with more than one selectable light jet are conflated to the last row. The distributions embody the accepted events after the first cut, corresponding to $\epsilon(\ell,t) = 46.33\,\%$ and $\epsilon(\ell,\bar{t}) = 47.88\,\%$.

The negative mass dependencies in the first columns and the comparably high positive values in the second columns in all distributions agree with the expectation, that with a higher top-quark mass the probability to encounter more b-tagged jets increases. A similar observation can be deduced from the first and second row, with regard to the relative mass dependencies of the light jet acceptances.

The selected centre-bins reveal that $38.6\,\%$ of top-quark events and $37.8\,\%$ of the top-antiquark events pass the jet selection for $p_T(j,b) = 30\,\mathrm{GeV}$. Interestingly, these numbers do not significantly change when using $p_T(j,b) = 20\,\mathrm{GeV}$. In case of the top-quark sets it decreases by $1\,\%$ and for the top-antiquark sets it increases by $0.2\,\%$. The reason for this is the shifting of events from the upper left to the lower right of the tables, respectively towards larger jet multiplicities. One the one hand, there are events that are selected at the higher threshold, but are not selected at the lower, because

j \ b	0	1	≥ 2
0	-2.24 (3.7 %)	+0.08 (17.4 %)	+0.43 (4.2 %)
1	-1.49 (8.8 %)	+0.20 (38.6 %)	+0.37 (9.8 %)
≥ 2	-0.09 (4.8 %)	+0.52 (8.7 %)	+0.53 (4.1 %)

TABLE 7.2: Relative mass dependencies $\bar{\delta}\,[\%/\mathrm{GeV}]$ distributed versus jet multiplicities using $pT_{b,j} > 30\,\mathrm{GeV}$. Parenthesised values add to $100\,\%$ corresponding to the acceptance of $46.33\,\%$ in the $(e+\mu)$-channel for top-quark sets.

j \ b	0	1	≥ 2
0	-2.34 (0.9 %)	-0.14 (9.0 %)	+0.13 (3.2 %)
1	-1.67 (4.4 %)	-0.01 (37.5 %)	+0.14 (13.2 %)
≥ 2	-0.22 (5.8 %)	+0.38 (16.6 %)	+0.40 (9.4 %)

TABLE 7.3: Relative mass dependencies $\bar{\delta}\,[\%/\mathrm{GeV}]$ distributed versus jet multiplicities using $pT_{b,j} > 20\,\mathrm{GeV}$. Parenthesised values add to $100\,\%$ corresponding to the acceptance of $46.33\,\%$ in the $(e+\mu)$-channel for top-quark sets.

j \ b	0	1	≥ 2
0	-2.34 (4.1 %)	+0.12 (19.1 %)	+0.33 (4.4 %)
1	-1.50 (9.0 %)	+0.22 (37.8 %)	+0.37 (9.4 %)
≥ 2	-0.25 (4.4 %)	+0.52 (8.1 %)	+0.63 (3.7 %)

TABLE 7.4: Relative mass dependencies $\bar{\delta}\,[\%/\mathrm{GeV}]$ distributed versus jet multiplicities using $pT_{b,j} > 30\,\mathrm{GeV}$. Parenthesised values add to $100\,\%$ corresponding to the acceptance of $47.88\,\%$ in the $(e+\mu)$-channel for top-antiquark sets.

j \ b	0	1	≥ 2
0	-2.30 (1.0 %)	-0.07 (9.8 %)	+0.01 (3.4 %)
1	-1.69 (4.5 %)	0.00 (38.0 %)	+0.09 (13.0 %)
≥ 2	-0.14 (5.6 %)	+0.40 (15.9 %)	+0.43 (8.8 %)

TABLE 7.5: Relative mass dependencies $\bar{\delta}\,[\%/\mathrm{GeV}]$ distributed versus jet multiplicities using $pT_{b,j} > 20\,\mathrm{GeV}$. Parenthesised values add to $100\,\%$ corresponding to the acceptance of $47.88\,\%$ in the $(e+\mu)$-channel for top-antiquark sets.

they have too many jets. One the other hand, there are events that are not selected at the higher threshold, because they have not enough jets, but can be selected at the lower threshold.

The resulting mass dependence in the selected bin amounts to $\bar{\delta}(t) = 0.20\,\frac{\%}{\mathrm{GeV}}$ and $\bar{\delta}(\bar{t}) = 0.22\,\frac{\%}{\mathrm{GeV}}$, which agrees to the results that can be deduced from the fits on the complete cut sequence presented in tables 6.2 and 6.3.

This analysis shows that by releasing the threshold on the jet minimum p_T to 20 GeV the mass dependence contributed by the jet selection effectively vanishes, since in the selected centre-bins $\bar{\delta}(t) = -0.01\,\frac{\%}{\mathrm{GeV}}$ and $\bar{\delta}(\bar{t}) = 0.00\,\frac{\%}{\mathrm{GeV}}$ can be achieved.

The impact on the final result observed for A_{fid} is presented in table 7.6 for top-quarks and in table 7.7 for top-antiquarks. With subsequently decreased values of $p_T(b)$ and $p_T(j)$, the acceptances vary for the described reasons, but the relative mass dependencies consequently decrease. This effect is stronger for $p_T(b)$ compared to $p_T(j)$ as expected.

pT_b	pT_j	$\bar{\epsilon}$	δ	$\bar{\delta}$
30 GeV	30 GeV	17.22	0.074	0.43
30 GeV	25 GeV	17.10	0.071	0.42
30 GeV	20 GeV	16.01	0.062	0.39
25 GeV	30 GeV	17.22	0.059	0.34
25 GeV	25 GeV	17.65	0.056	0.32
25 GeV	20 GeV	16.55	0.047	0.28
20 GeV	30 GeV	16.89	0.048	0.28
20 GeV	25 GeV	17.30	0.043	0.25
20 GeV	20 GeV	16.93	0.035	0.21

TABLE 7.6: Fiducial acceptances and mass dependencies for lowered minimum pT threshold for both jets calculated for top-quark sets.

pT_b	pT_j	$\bar{\epsilon}$	δ	$\bar{\delta}$
30 GeV	30 GeV	17.46	0.076	0.44
30 GeV	25 GeV	17.59	0.074	0.42
30 GeV	20 GeV	16.71	0.064	0.38
25 GeV	30 GeV	17.53	0.060	0.34
25 GeV	25 GeV	18.18	0.056	0.31
25 GeV	20 GeV	17.32	0.047	0.27
20 GeV	30 GeV	17.25	0.048	0.28
20 GeV	25 GeV	17.89	0.042	0.24
20 GeV	20 GeV	17.72	0.034	0.19

TABLE 7.7: Fiducial acceptances and mass dependencies for lowered minimum pT threshold for both jets calculated for top-antiquark sets.

8. Conclusion

The method and the applicability of an indirect top-quark mass measurement using top-quark production cross-sections has been theorised and analysed in this work. It has been argued that the measurement strategy strongly depends on the distinction between the mass dependencies of the theoretically predicted and the measured cross-sections.

Theory calculations in next-to-leading order, extracted from the Hathor program, have been presented and discussed. They were used to provide the xHathor program that produces the presented plots and data. It has been concluded from the comparison to pair-production and to the other production channels of single top-quarks that in the t-channel a much weaker mass dependence is observed. The best channel for the top-quark mass extraction, with respect to the mass dependence of the predicted cross-section, would be the s-channel. Unfortunately, this is the channel with the lowest production rates at the LHC.

Experimentally obtained results for the inclusive t-channel top-quark cross-section using the ATLAS detector have been presented and the applied fiducial measurement technique has been described. It has been shown, that the mass dependence of the ATLAS result is not suitable for the indirect top-quark mass extraction, because it amounts to a value that lies too close to the theoretical predictions. In fact, the mass dependence with $d\sigma(tq+\bar{t}q)/dm = -1.07\,\%/\mathrm{GeV}$ is even a bit larger than the predicted that is $d\sigma(tq+\bar{t}q)/dm = -0.9\,\%/\mathrm{GeV}$.

In order to provide an ansatz to reduce the experimental mass dependence, it has been argued that it can be related to the contributions of two decoupled sub-processes. The measurement of the fiducial cross-section exhibits a mass dependence that depends on the reconstruction efficiency and the neural network fit. This has not been further detailed in this thesis. The second part relates to the extrapolation to the full phase space and emerges from the simulation of the fiducial acceptance. Techniques to analyse particular sources of the mass dependence of this process have been elaborated.

It has been concluded that with an extension of the observed phase towards lower pT regions, at least parts of the mass dependence can be removed. This is not applicable for the observation made for the simulation of the electron selection, due to HLT limitations. For the comparably stronger observation, that the mass dependence on the jet selection can be removed completely, a certain perspective for further research might have been found.

This motivates to outline strategies to minimise the request for the jet minimum transverse momentum in fiducial cross-section measurements using the ATLAS detector at the LHC.

However, it is clearly conclusive from this work, that the accuracy of the indirect top-quark mass measurement from singly produced cross-sections

can not be expected to reach the precision of the direct reconstruction methods and will unlikely produce competitive results. Still, it provides a theoretically clear and interesting insight into various aspects of top-quark mass and cross-section studies.

A. Mass extraction from s-channel and Wt-production

A.1 s-channel

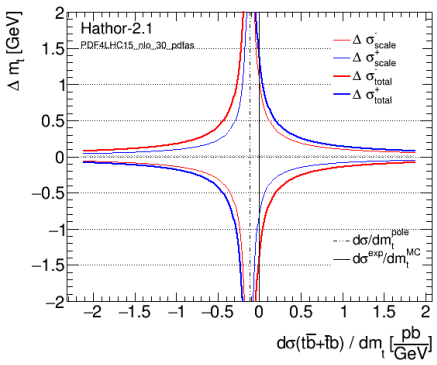

FIGURE A.1: Accuracy of the indirect top-quark pole mass measurement versus experimental mass dependence

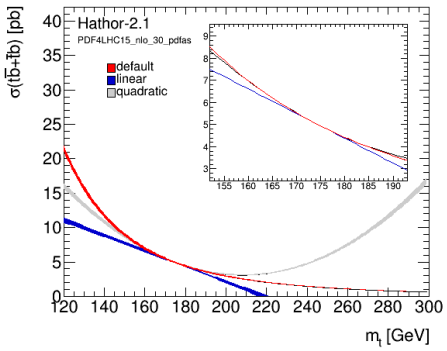

FIGURE A.2: Extrapolation of cross-section predictions and total uncertainty

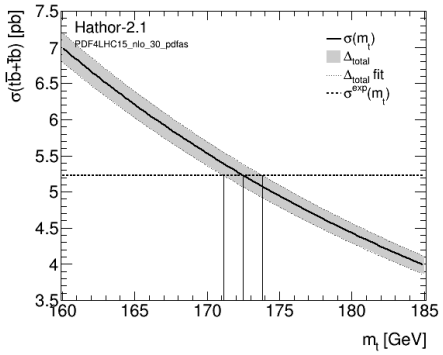

FIGURE A.3: Intersection of theorised curve with an idealised mass-independent measurement

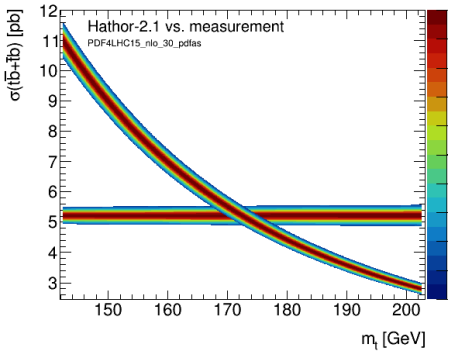

FIGURE A.4: Pseudo experiments for the theorised curve and an idealised mass-independent measurement

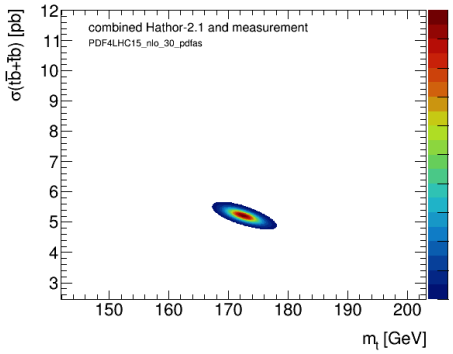

FIGURE A.5: Likelihood of theory results and an idealised measurement

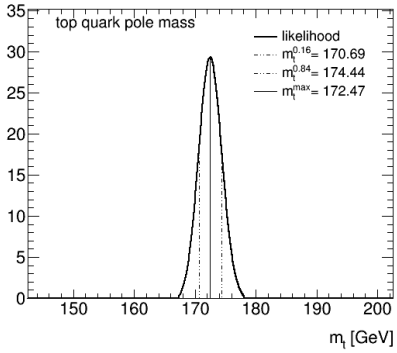

o

FIGURE A.6: Mass extraction frm the projected likelihood

A.2 Wt-channel

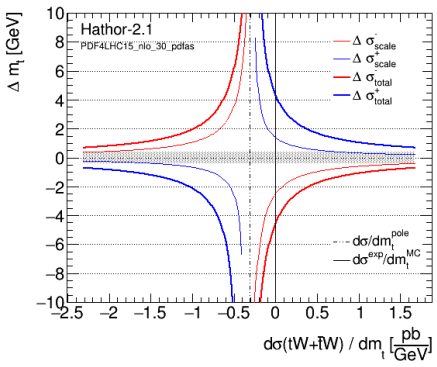

FIGURE A.7: Accuracy of the indirect top-quark pole mass measurement versus experimental mass dependence

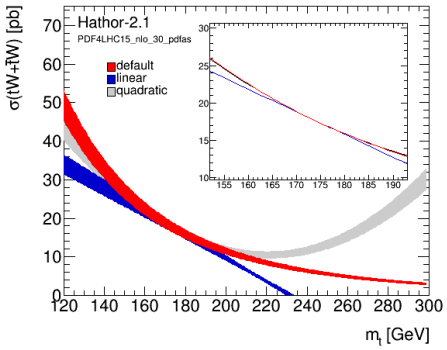

FIGURE A.8: Extrapolation of cross-section predictions and total uncertainty

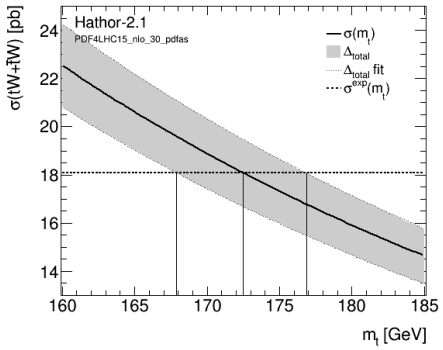

FIGURE A.9: Intersection of theorised curve with an idealised mass-independent measurement

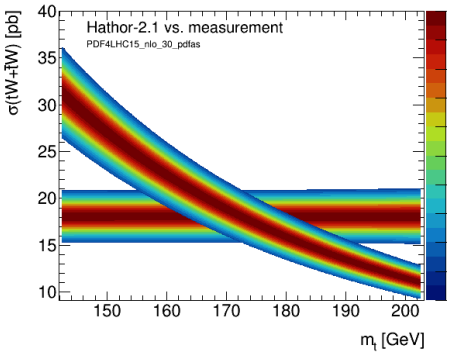

7

(a) Pseudo experiments for the theorised curve and an idealised mass-independent measurement

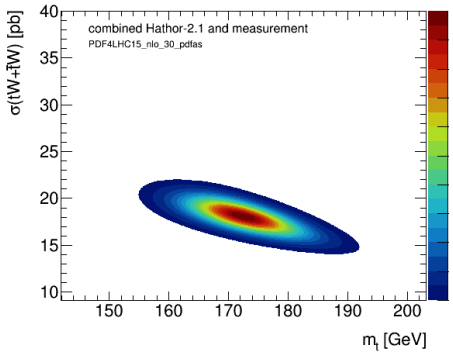

FIGURE A.11: Likelihood of theory results and an idealised measurement

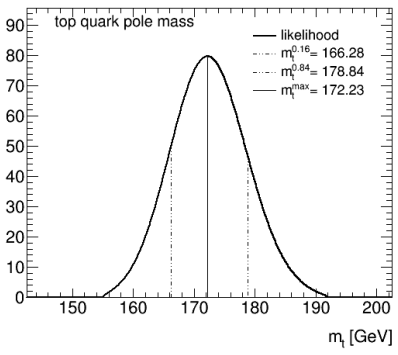

FIGURE A.12: Mass extraction from the projected likelihood

B. xHathor parameter list

Options	description
-h [–help]	Print help message
-v [–verbose]	Print more messages
–debug	Print debug messages
-x [–axis] arg	Choose axis from **m** for $m_t = 165$ -$180\,\mathrm{GeV}$ **M** for $m_t = 165$ -$950\,\mathrm{GeV}$ **s** for $\sqrt{s} = 1.8$ -$14\,\mathrm{TeV}$
-a [–accuracy] arg	Accuracy: **low** (default), **medium** ,**high**
-c [–channel] arg	Channel: **t** (default), **s** ,**Wt**
-d [–degree] arg	Degree for fit functions: **0** (default: equation 3.13), **1** linear ,**2** quadratic
-f [–file] arg	configuration file name (default is XS.config)
-i [–ignore]	ignore cached data
-I [–overwrite]	overwrite cached data
–MCn arg	MC-data of linear fit at $172.5\,\mathrm{GeV}$
–MCm arg	MC-data slope m of linear fit
–MCs arg	MC-data sigma of linear fit
-o [–out] arg	Output folder (default is ./output)
–data arg	data cache folder (default is ./datacache)
-p [–pdf] arg	Choose a PDF Set from **PDF4LHC**: PDF4LHC15_nlo_30_pdfas (default) **CT14** = CT14nlo **NNPDF** = NNPDF30_nlo_as_0118 **MMHT** = MMHT2014nlo68cl or choose one of the installed pdf sets
-P [–pdfs] arg	More than one PDF set separated by comma example: **CT14,NNPDF,MMHT**
-q [–quark] arg	Choose particle from **both** (default), **top**, **antitop**
-s [–energy] arg	Centre-of-mass energy (default: $\sqrt{s} = 8000$)
–mt arg	Reference top-quark mass (default: $172.5\,\mathrm{GeV}$)
-u [–unc] arg	uncertainty calulation with **L** LHAPDF6.1.6 (default) **H** Hathor-2.1-b3

TABLE B.1: Available Command Line Parameters implemented in the xHathor program. More documentation can be found in the source code.

Bibliography

[1] M Beneke et al. "On the ultimate uncertainty of the top quark pole mass" (2016). arXiv: 1605.03609 [hep-ph].

[2] Mathias Butenschoen, Bahman Dehnadi, Andre H. Hoang, Vicent Mateu, Moritz Preisser, Iain W. Stewart. "Top Quark Mass Calibration for Monte Carlo Event Generators" (2016). arXiv: 1608.01318v1 [hep-ph].

[3] The ATLAS Collaboration. "Measurement of the $t\bar{t}$ production cross-section using $e\mu$ events with b-tagged jets in pp collisions at $\sqrt{s} =$ 7 TeV and 8 teV with the ATLAS detector" (2014). arXiv: 1406.5375v2 [hep-ph].

[4] CMS Collaboration. "Determination of the top-quark pole mass and strong coupling constant from the $t\bar{t}$ production cross section in pp collisions at $\sqrt{s} = 7$ TeV". Phys. Lett. B 728 496 (2014). URL: arXiv: 1307.1907v4.

[5] Thomas Schöerner-Sadenius, ed. *Harvest of run 1*. Springer International Publishing Switzerland, 2015. DOI: 10.1007/978-3-319-15001-7.

[6] Marcel Vos. "Top-quark mass measurements at the LHC: alternative methods" (2016). arXiv: 1602.00428v2 [hep-ph].

[7] The D∅ Collaboration. "Measurement of the $t\bar{t}$ production cross section using dilepton events in $p\bar{p}$ collisions" (2011). arXiv: 1105.5384v2 [hep-ph].

[8] The D∅ Collaboration. "Measurement of the inclusive $t\bar{t}$ production cross section in $p\bar{p}$ collisions at 1.96 TeV and determination of the top quark pole mass" (2016). arXiv: 1605.06168v1 [hep-ph].

[9] ATLAS Collaboration. "Combined measurement of the Higgs Boson mass in pp collisions at $\sqrt{s} = 7$ and $\sqrt[8]{TeV}$ with the ATLAS and CMS experiments". Phys. Rev. Lett. 114 191803 (2015). arXiv: arXiv: 1503.07589 [hep-ph].

[10] "Image reference" (2014). URL: https://commons.wikimedia.org/wiki/File:Standard_Model_of_Elementary_Particles.svg.

[11] Makoto Kobayashi and Toshihide Maskawa. "CP Violation in the Renormalizable Theory of Weak Interaction". *Prog. Theor. Phys.* 49 (1973), pp. 652–657. DOI: 10.1143/PTP.49.652.

[12] "Image reference" (2013). URL: https://commons.wikimedia.org/wiki/File:Weak_Decay_(flipped).svg.

[13] "The CKM quark mixing matrix". Particle Data Group - Reviews (2016). URL: http://pdg.lbl.gov/2016/mobile/reviews/pdf/rpp2016-rev-ckm-matrix-m.pdf.

[14] The ATLAS and CMS Collaborations. "Combination of ATLAS and CMS results on the mass of the top quark using up to $4.9\,\mathrm{fb}^{-1}$ of data" (2012). URL: https://cds.cern.ch/record/1460441/files/ATLAS-CONF-2012-095.pdf.

[15] The Tevatron Electroweak Working Group. "Combination of CDF and D∅ results on the mass of the top quark using up to $9.7\,\mathrm{fb}^{-1}$ at the Tevatron" (2014). arXiv: 1407.2682 [hep-ph].

[16] CMS The ATLAS CDF and D∅ Collaborations. "First combination of Tevatron and LHC measurements of the top-quark mass" (2014). arXiv: 1403.4427 [hep-ph].

[17] ARGUS COLLABORATION. "Observation of B0 - anti-B0 Mixing". DESY 87-029 (Apr. 1987). URL: http://www-library.desy.de/report87.html.

[18] CDF Collaboration. "Observation of Electroweak Single-Top Quark Production". Phys. Rev. Lett. 103 (2009). arXiv: 0903.0885 [hep-ph].

[19] D∅ Collaboration. "Observation of Single Top-Quark Production". Phys. Rev. Lett. 103 (2009). arXiv: 0903.0850 [hep-ph].

[20] M. Jezabek. "Top Quark Physics" (1994). arXiv: 9406411 [hep-ph].

[21] The CMS Collaboration. "Measurement of the W boson helicity fractions in the decays of top quark pairs to lepton+jets final states produced in pp collisions at $\sqrt{s} = 8\,\mathrm{GeV}$" (2016). arXiv: 1605.09047 [hep-ph].

[22] Werner Bernreuther, Dennis Heisler, Zong-Guo Si. "A set of top quark spin correlation and polarization observables for the LHC: Standard Model predictions and new physics contributions" (2015). arXiv: 1508.05271v2 [hep-ph].

[23] The CMS and LHCb Collaborations. "Observation of the rare $B_s^0 \to \mu^+\mu^-$ decay from the combined analysis of CMS and LHCb data" (2014). arXiv: 1411.4413 [hep-ph].

[24] L. Di Luzio,G. Isidori, G. Ridolfi. "Stability of the electroweak ground state in the Standard Model and its extensions". *Phys. Lett. B* 753 (2016). DOI: 10.1016/j.physletb.2015.12.009.

[25] G. Degrassi, S. Di Vita, J. Elias-Miro, J.R. Espinosa, G.F. Giudice et al. "Higgs mass and vacuum stability in the Standard Model at NNLO". *High Energy Phys* 1208 (2012). DOI: 10.1007/JHEP08(2012)098. arXiv: 1205.6497 [hep-ph].

[26] D. Buttazzo, G. Degrassi, P.P. Giardino, G.F. Giudice, F.Sala et al. "Investigating the near-criticality of the iggs boson". *High Energy Phys* 1312 (2012). DOI: 10.1007/JHEP12(2013)089. arXiv: 1307.3536 [hep-ph].

[27] "Single top quark production as a window to physics beyond the Standard Model". Phys Rev. D63 (2001). URL: doi:10.1103/PhysRevD.63.014018.

[28] John M. Campbell et al. "Next-to-Leading-Order Predictions for t-Channel Single-Top Production at Hadron Colliders". *Phys. Rev. Lett.* 102 (2009). arXiv: 0903.0005.

[29] Nikolaos Kidonakis. "Next-to-next-to-leading-order collinear and soft gluon corrections for t-channel single top quark production". *Phys. Rev. D* 83 (2011), p. 091503. DOI: 10.1103/PhysRevD.83.091503. arXiv: 1103.2792 [hep-ph].

[30] Nikolaos Kidonakis. "NNLL resummation for s-channel single top quark production". *Phys. Rev. D* 81 (2010), p. 054028. DOI: 10.1103/PhysRevD.81.054028. arXiv: 1001.5034 [hep-ph].

[31] Nikolaos Kidonakis. "Two-loop soft anomalous dimensions for single top quark associated production with a W^- or H^-". *Phys. Rev. D* 82 (2010), p. 054018. DOI: 10.1103/PhysRevD.82.054018. arXiv: 1005.4451 [hep-ph].

[32] Mathias Brucherseifer, Fabrizio Caola, and Kirill Melnikov. "On the NNLO QCD corrections to single-top production at the LHC". *Phys. Lett. B* 736 (2014), pp. 58–63. DOI: 10.1016/j.physletb.2014.06.075. arXiv: 1404.7116 [hep-ph].

[33] Andrea Giammanco. "Single top quark production at the LHC" (2015). arXiv: 1511.06748v2 [hep-ph].

[34] "Image reference" (2016). URL: atlas.web.cern.ch/Atlas/GROUPS/PHYSICS/CombinedSummaryPlots/TOP/singletop_allchanvsroots_ATLASonly/singletop_allchanvsroots_ATLASonly.png.

[35] The D∅ Collaboration. "Observation of Single Top-Quark Production" (2009). arXiv: 0903.0850 [hep-ph].

[36] The CDF Collaboration. "First Observation of Electroweak Single Top Quark Production" (2009). arXiv: 0903.0885 [hep-ph].

[37] The CDF Collaboration. "Observation of Top Quark Production in Pbar-P Collisions" (1995). arXiv: 9503002 [hep-ph].

[38] The D∅ Collaboration. "Observation of the Top Quark" (1995). arXiv: 9503003 [hep-ph].

[39] The CDF Collaboration The D∅ Collaboration. "Tevatron Combination of Single-Top-Quark Cross Sections and Determination of the Magnitude of the Cabibbo-Kobayashi-Maskawa Matrix Element V_{tb}" (2015). arXiv: 1503.05027 [hep-ph].

[40] The ATLAS Collaboration. "Measurement of the inclusive cross-sections of single top-quark and top-antiquark t-channel production in pp-collisions at $\sqrt{s} = 13\,\mathrm{TeV}$ with the ATLAS detector" (2016). arXiv: 1609.03920 [hep-ph].

[41] "Measurement of the differential cross section for t-channel single-top-quark production at $\sqrt{s} = 13\,\mathrm{TeV}$". CMS-PAS-TOP-16-004 (2016). URL: https://cds.cern.ch/record/2151074/files/TOP-16-004-pas.pdf.

[42] P. Kant et al. "HATHOR for single top-quark production: Updated predictions and uncertainty estimates for single top-quark production in hadronic collisions" (2014). URL: arXiv:1406.4403[hep-ph].

[43] Andy Buckley, James Ferrando, Stephen Lloyd, Karl Nordström, Ben Page, Martin Rüfenacht, Marek Schönherr, Graeme Watt. "LHAPDF6: parton density access in the LHC precision era" (2014). DOI: 10.1140/epjc/s10052-015-3318-8. arXiv: 1412.7420v2 [hep-ph].

[44] J. Campbell, R. Ellis, and F. Tramontano. "Single Top Production and Decay at Next-To-Leading Order". Phys. Rev. D70 (2004) 094012 (2004). arXiv: hep-ph/0408158 [hep-ph].

[45] J. Campbell and F. Tramontano. "Next-To-Leading Order Corrections to Wt Production and Decay". Nucl. Phys. B726 (2005). arXiv: hep-ph/0506289 [hep-ph].

[46] "A New Algorithm for Adaptive Multidimensional Integration". J.Comput.Phys. 27, 192 (1978).

[47] "VEGAS: AN ADAPTIVE MULTIDIMENSIONAL INTEGRATION PROGRAM" (1978).

[48] "MCFM – Monte Carlo for FeMtobarn Processes, Version 6.5" (2013). URL: http://mcfm.fnal.gov.

[49] Thomas Kintscher. "Fast Single-Top Cross-Section Predictions for Hadron Colliders with the HATHOR Program" (2013). URL: https://www.physik.hu-berlin.de/de/eephys/ATLAS/theses/pdfs/ma_thesis_kintscher.pdf.

[50] *ATLAS-CMS recommended predictions for single-top cross sections using the Hathor v2.1 program*. URL: https://twiki.cern.ch/twiki/bin/view/LHCPhysics/SingleTopRefXsec.

[51] Jon Butterworth, Stefano Carrazza, Amanda Cooper-Sarkar, Albert De Roeck, Joel Feltesse, Stefano Forte, Jun Gao, Sasha Glazov, Joey Huston, Zahari Kassabov, Ronan McNulty, Andreas Morsch, Pavel Nadolsky, Voica Radescu, Juan Rojo, Robert Thorne. "PDF4LHC recommendations for LHC Run IIC" (2015). arXiv: 1510.03865 [hep-ph].

[52] Sergey Alekhin, Simone Alioli, Richard D. Ball, Valerio Bertone, Johannes Blümlein, Michiel Botje, Jon Butterworth, Francesco Cerutti, Amanda Cooper-Sarkar, Albert de Roeck, Luigi Del Debbio, Joel Feltesse, Stefano Forte, Alexander Glazov, Alberto Guffanti,Claire Gwenlan, Joey Huston, Pedro Jimenez-Delgado, Hung-Liang Lai, José I. Latorre, Ronan McNulty, Pavel Nadolsky, Sven Olaf Moch, Jon Pumplin, Voica Radescu, Juan Rojo, Torbjörn Sjöstrand, W.J. Stirling, Daniel Stump, Robert S. Thorne, Maria Ubiali, Alessandro Vicini, Graeme Watt, C.-P. Yuan. "The PDF4LHC Working Group Interim Report" (2011). arXiv: 1101.0536 [hep-ph].

[53] Dulat,S and Hou, T.J. and Gao,J. and Guzzi,M. and Huston,J. and Nadolsky,P. and Pumplin,J, and Schmidt,C. and Stump,D. and Yuan,C.P. "The CT14 Global Analysis of Quantum Chromodynamics" (2015). arXiv: 1506.07443 [hep-ph].

[54] P. Motylinski L. A. Harland-Lang A. D. Martin and R.S. Thorne. "Parton distributions in the LHC era: MMHT 2014 PDFs" (2015). arXiv: 1412.3989 [hep-ph].

[55] R.D. Ball et al. "Parton Distributions for the LHC Run II" (2015). arXiv: 1410.8849 [hep-ph].

[56] G. Watt. "Parton distribution function dependence of benchmark Standard Model total cross sections at 7 TeV LHC" (2011). arXiv: 1106.5788v2 [hep-ph].

[57] Michal Czakon, Paul Fiedler, Alexander Mitov. "The total top quark pair production cross-section at hadron colliders through $\mathcal{O}(\alpha_S^4)$" (2013). DOI: 10.1103/PhysRevLett.110.252004. arXiv: arXiv:1303.6254 [hep-ph].

[58] Fabian-Phillipp Tepel et al. *Measurement of the Inclusive and Fiducial Cross-Section in Single Top-Quark t-Channel Events in pp Collisions at* $\sqrt{s} = 8\,\mathrm{TeV}$. Tech. rep. ATL-COM-PHYS-2015-177. Geneva: CERN, 2015. URL: https://cds.cern.ch/record/1999237.

[59] Michael Schuh. "A study of the luminosity zone of the ATLAS detector at the LHC". CERN-Thesis-2012-106 (2012).

[60] ATLAS Collaboration. "Measurement of the Inclusive and Fiducial Cross-Section of Single Top-Quark t-Channel Events in pp Collisions at $\sqrt{s} = 8\,\mathrm{TeV}$". ATLAS-CONF-2014-007 (2014). URL: http://cdsweb.cern.ch/record/1668960.

[61] ATLAS Collaboration. "Measurement of t-Channel Single Top-Quark Production in pp Collisions at $\sqrt{s} = 8\,\mathrm{TeV}$ with the ATLAS detector". ATLAS-CONF-2012-132 (2012). URL: http://cdsweb.cern.ch/record/1478371.

[62] "Image reference" (2016). URL: https://inspirehep.net/record/1356996/files/atlas.png.

[63] *ATLAS detector and physics performance: Technical Design Report, 1*. Technical Design Report ATLAS. Geneva: CERN, 1999. URL: https://cds.cern.ch/record/391176.

[64] "Expected Performance of the ATLAS Experiment - Detector, Trigger and Physics" (2009). arXiv: 0901.0512 [hep-ph].

[65] "Image reference" (2016). URL: http://www.spontaneoussymmetry.com/work/atlas.

[66] "Image reference" (2016). URL: https://inspirehep.net/record/871877/files/FigID11blast_1.png.

[67] ATLAS Collaboration. "Electron performance measurements with the ATLAS detector using the 2010 LHC proton-proton collision data" (2011). arXiv: arXiv:1110.3174 [hep-ph].

[68] "Image reference" (2014). URL: https://en.wikipedia.org/wiki/B-tagging#/media/File:B-tagging_diagram.png.

[69] The ATLAS Collaboration. "Performance of b-Jet Identification in the ATLAS Experiment" (2016). arXiv: 1512.01094v2 [hep-ph].

[70] "Image reference" (2016). URL: https://twiki.cern.ch/twiki/pub/AtlasPublic/EventDisplayRun2Collisions/run267073_evt279124678-thumb.png.

[71] "Efficient Identification of Boosted Semileptonic Top Quarks at the LHC" (2011). arXiv: 1007.2221 [hep-ph].

[72] "Improved luminosity determination in pp collisions at $\sqrt{s} = 7\,\mathrm{TeV}$ using the ATLAS detector at the LHC" (2013). arXiv: 1302.4393 [hep-ph].

[73] S. Alioli et al. "A general framework for implementing NLO calculations in shower Monte Carlo programs: the POWHEG BOX" (2010). arXiv: 1002.2581v1 [hep-ph].

[74] T. Sjöstrand et al. "An Introduction to PYTHIA 8.2" (2014). arXiv: 1410.3012 [hep-ph].

[75] S. Frixione, P. Nason, and C. Oleari. "Matching NLO QCD computations with Parton Shower simulations: the POWHEG method" (2007). arXiv: 0709.2092 [hep-ph].

[76] T Bintoh et al., eds. *LHC Physics*. CRC Press, Scottish Graduate Series, 2012.

[77] The ATLAS collaboration. "Performance of the ATLAS muon trigger in pp collisions at $\sqrt{8}\,\mathrm{TeV}$" (2015). arXiv: 1408.3179v2 [hep-ph].

[78] The ATLAS collaboration. "Electron and photon trigger performance measurements using 2012 ATLAS data". ATL-COM-DAQ-2014-058 (2014). URL: https://cds.cern.ch/record/1706278.

[79] "Data-Quality Requirements and Event Cleaning for Jets and Missing Transverse Energy Reconstruction with the ATLAS Detector in Proton–Proton Collisions at a Center-of-Mass Energy of $\sqrt{7}\,\mathrm{TeV}$" (2010). URL: http://cdsweb.cern.ch/record/1277678.